12-1-2015

An Approach to Model Plastic Deformation of Metallic Plates in Hypervelocity Impact Experiments

Shawoon Kumar Roy
University of Nevada, Las Vegas, roys8@unlv.nevada.edu

AN APPROACH TO MODEL PLASTIC DEFORMATION OF METALLIC PLATES IN HYPERVELOCITY IMPACT EXPERIMENTS

By

Shawoon Kumar Roy

Bachelor of Science - Materials and Metallurgical Engineering
Bangladesh University of Engineering and Technology
July 2008

Master of Science - Materials and Nuclear Engineering
University of Nevada, Las Vegas
July 2011

A dissertation submitted in partial fulfillment
of requirements for the

Doctor of Philosophy in Engineering -Mechanical Engineering

Department of Mechanical Engineering
Howard R. Hughes College of Engineering
The Graduate College

University of Nevada, Las Vegas
December 2015

UNLV | GRADUATE COLLEGE

Dissertation Approval

The Graduate College
The University of Nevada, Las Vegas

September 4, 2015

This dissertation prepared by

Shawoon Kumar Roy

entitled

An Approach to Model Plastic Deformation of Metallic Plates in Hypervelocity Impact Experiments

is approved in partial fulfillment of the requirements for the degree of

Doctor of Philosophy in Engineering – Mechanical Engineering
Department of Mechanical Engineering

Mohamed Trabia, Ph.D.
Examination Committee Co-Chair

Brendan O'Toole, Ph.D.
Examination Committee Co-Chair

Robert Hixson, Ph.D.
Examination Committee Member

Yitung Chen, Ph.D.
Examination Committee Member

William Culberth, Ph.D.
Examination Committee Member

Zhiyong Wang, Ph.D.
Examination Committee Member

Rama Venkat, Ph.D.
Graduate College Faculty Representative

Kathryn Hausbeck Korgan, Ph.D.
Graduate College Interim Dean

ABSTRACT

An Approach to Model Plastic Deformation of Metallic Plates in Hypervelocity Impact Experiments

by

Shawoon Kumar Roy

Dr. Mohamed B. Trabia, Examination Committee Chair
Associate Dean for Research, Graduate Studies, and Computing
Professor of Mechanical Engineering
University of Nevada, Las Vegas

Dr. Brendan J. O'Toole, Examination Committee Chair
Professor of Mechanical Engineering
University of Nevada, Las Vegas

Space structures are subjected to micro-meteorite impact at extremely high velocities of several kilometers per second. Similarly, design of military equipment requires understanding of material behavior under extremely high pressure and temperature. Study of material behavior under hypervelocity impact (HVI) poses many challenges since few researchers so far have approached this problem. Material models, equations of the state, and fracture mechanics are not well-understood under these conditions.

The objective of this research is to present an approach for studying plastic deformation of metallic plates under HVI conditions. A two-stage light gas gun can be used to simulate these conditions under controlled experimental conditions. In all gas gun experiments, projectiles are driven by light gas propellants (typically Hydrogen or Helium) to impact target plates. These experiments, which typically last few microseconds, are associated with large localized

deformation, which makes capturing data challenging. Additionally, the resulting shock waves create several failure modes simultaneously such as formations of spalls, petals, discs, and plugs in target plates. These failure modes are mostly controlled by several factors such as impact velocity, material properties, projectile and target geometry, etc.

In this work, plastic deformation is related to the velocities at multiple points on the back surface of the impacted plate. These velocities are measured using a multi-channel Multiplexed Photonic Doppler Velocimetry (MPDV)[1] diagnostic system, which is an interferometric fiber-optic technique that can determine the velocity of a point by measuring the Doppler shift of light reflected from a moving surface.

These experiments are simulated using the Lagrangian-based smooth particle hydrodynamics (SPH) solver in LS-DYNA. Simulation models use Johnson-Cook material model with Mie-Grüneisen equation of state (EOS).

To assess the proposed approach, preliminary testing was conducted using 12.7 mm (0.5 inch) thick ASTM A36 steel plates, which were impacted by cylindrical Lexan projectiles at velocities ranging from 4.5 to 6 km/s. Impact typically created a small crater in the front of the plate and a bulge on the back surface which usually led to fracture near the crate and spallation of material inside the plate. In addition to recoding impact velocity, back surface velocities were recorded, and crater details were measured.

Several simulation models were developed with the objective of producing simulation results that are close to experimental ones. Simulation results were assessed based on comparison physical damage and velocity profiles. Adjustment of the simulation model included varying the parameters

[1] In collaboration with the staff of National Security Technologies LLC

of the Johnson-Cook material model, EOS, and bulk viscosity, choosing appropriate spall model, and tuning particle spacing.

Initial experiments with A36 steel showed reasonable success to use the MPDV system. Further experiments were planned to design with better MPDV arrangement. Two other different steels ware studied in: 304L and HY100. Simulation of these experiments were also compared with MPDV results to better understand material model behavior.

ACKNOWLEDGEMENTS

First, I would like to thank every people who made this dissertation possible. This dissertation is dedicated to my parents who have always inspired me through this long period. My gratitude can't be expressed in words to my advisors Dr. Mohamed Trabia and Dr. Brendan O'Toole for their enormous help and guidance throughout the project.

Also, I would like to thank all my committee members Dr. Robert Hixson, Dr. Yitung Chen, Dr. William Culberth, Dr. Zhiyong Wang and Dr. Rama Venkat for their invaluable time in reviewing this dissertation and participating in dissertation presentation. My sincere thanks extends to all the research stuffs and number of students who made this long journey in UNLV possible. I would like to thank Jagadeep, Deepak, Richard, Melissa who had been actively supportive during this entire PhD study.

This study was conducted by National Security Technologies, LLC, under Contract No. DE-AC52-06NA25946 with the U.S. Department of Energy, and supported by the Site-Directed Research and Development Program. I would also like to thank Dr. Ed Daykin, Steven Becker, Michael Peña, Michael Walling and all other NSTec members for their help and support throughout the project.

Lastly, I offer my regards and love to my beloved younger sister, my wife, my relatives, my friends and all other people who supported me finishing the project.

TABLE OF CONTENTS

LIST OF TABLES

LIST OF FIGURES

CHAPTER 1 INTRODUCTION

1.1 Literature Review

Hypervelocity impact events are ubiquitous in many areas, including micro-meteoroid collision with spacecraft, projectile impacts, and when modeling effects of explosives on structures. Consequently, researchers have been studying various aspects of this problem for several decades. A common technique to study hypervelocity impact in laboratory settings is the two-stage light-gas gun [1,2] , which can accelerate a projectile to generate shock waves in a target that are similar to those created by detonating high explosives or meteorite collisions [3]. Swift [4] discussed the historical development of this type of gun.

Under hypervelocity impact conditions, thin metallic plates tend to stretch and bend around the impact area, absorbing a significant part of the projectile's kinetic energy before perforation occurs. On the other hand, thick plates experience several failure modes during impact, such as spalling, petalling, discing, and plugging [5]. These failure modes depend upon several factors, such as the impact velocity, the properties of the plate material, and the geometry of the projectile.

Spalling, which is of a particular interest in this study, occurs when a triangular-shaped stress wave is reflected from the back of the target plate, thereby creating a tensile pressure that is greater than the material strength [6], which then results in an internal crack that progresses normal to the direction of the wave. Spall is a dynamic process and the maximum tensile pressure attained during this process is referred to as 'spall strength' of the material.

Failure modes for rod penetration experiments under hypervelocity impact conditions have been studied only by a relatively small number of researchers [7]. Goldsmith et al. [8] studied and described analytically the elastic-plastic plate deformation of aluminum plates impacted by a hard-steel cylindrical-nose projectile. Christman and Gehrig [9] studied the penetration mechanics and cratering processes in metallic and nonmetallic targets at impact velocities from 0.3 to 6.7 km/s. Subsequent studies on spall fracture and dynamic response of materials were reviewed by Oscarson and Graff [6]. Shockey et al. [10] reported that different projectile materials cause different types of physical damage to steel plates under hypervelocity impact. In addition, they reported microstructural changes and the pressure induced $\alpha \rightleftarrows \varepsilon$ polymorphic transition of the steel plates during impact.

Bond [11] suggested that spallation damage and phase-transition kinetics were important in damage studies of martensitic steel armor when subjected to hypervelocity impact. Merzhievskii and Titov [12] evaluated the perforation and deformation of thin steel plates at velocities from 3 to 9 km/s; they developed an analytical method to relate debris particles to the impact velocity. Johnson and Cook [13] developed a constitutive model for materials subjected to large strains, high strain rates, and high temperatures. Sorensen et al. [14] studied penetration mechanics of semi-infinite rolled homogeneous armor (RHA) steel by monolithic projectiles and segmented penetrators at velocities ranging from 2.5 to 4.0 km/s. The penetration behavior of long-rod tungsten-alloy projectiles in high-hard armor steel plates was studied by Anderson et al. [15] at two impact velocities, 1.25 km/s and 1.70 km/s. The ballistic limits of aluminum plates of various thicknesses were studied by Børvik et al. [16] using a compressed-air gas gun. An analytical model was developed based on those limits. Although this type of hypervelocity research have been conducted for several decades, only few of them tried to study plastic deformation of metallic

plates besides different failure mechanisms of different materials. Hence, a detail understanding of deformation mechanism of metallic plates in such extreme conditions demands a significant attention in research still.

Most of the early experimental work in impact dynamics and shock physics were conducted with relatively simple diagnostic systems. Part of this was due to the complexity of the experiment and lack of sophisticated diagnostics technologies; these took decades to develop. Therefore, significant effort was taken in the past few decades to develop new and accurate diagnostic systems to acquire data from this type of dynamic experiments. Recent work on impact dynamics and shock physics of materials emphasized the use of velocimetry data in flyer plate experiments to characterize the equation of state, spall strength, polymorphic phase transition, and the Hugoniot elastic limit of materials. Velocimetry data can provide a clear representation of the response of materials under high pressure and high strain rates, which may lead to developing accurate predictive computational models for materials. The following is a brief overview of velocimetry diagnostic techniques.

Barker and Hollenbach developed the homodyne interferometry technique: Velocity Interfero-meter System for Any Reflector (VISAR) system [17]. Typically a VISAR system collects velocimetry data by using an interferometer to measure the minute Doppler shift in light frequency given to a light beam as it is reflected by moving target surface. This technique became widely popular within the shock physics community. Numerous impact and shock studies have used VISAR as the primary diagnostic tool [18–26]. A typical flowchart of VISAR system measurement is presented in Figure 1.1 (recreated from [27]).

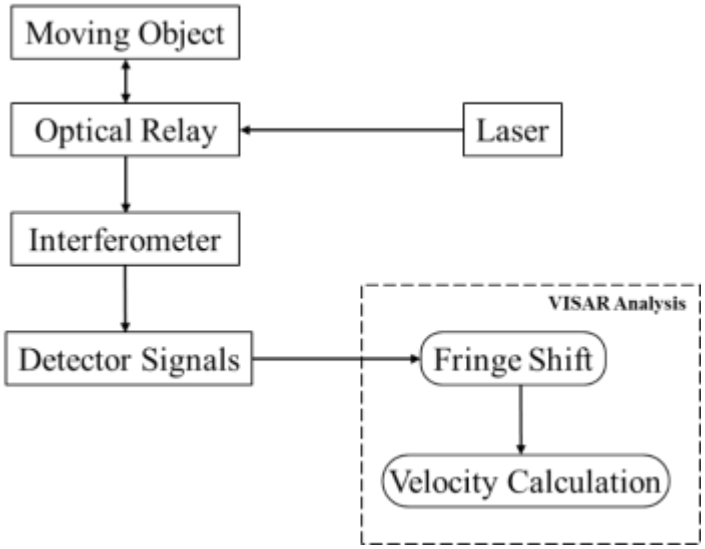

Figure 1.1 Overview of a VISAR Measurement

However, complexity, cost, and various issues that cannot be easily resolved, such as obtaining velocities from multiple points on a moving surface, prompted the development of an alternative diagnostic tool known as photonic Doppler velocimetry (PDV) [28]. Concept of PDV was first introduced by Strand et al. [28] which is a heterodyne velocimetry system. PDV is a displacement interferometer that collects velocity data based on measuring displacement using optical fiber probes. Typical flowchart of PDV system measurement is presented below in Figure 1.2 recreated from [28].

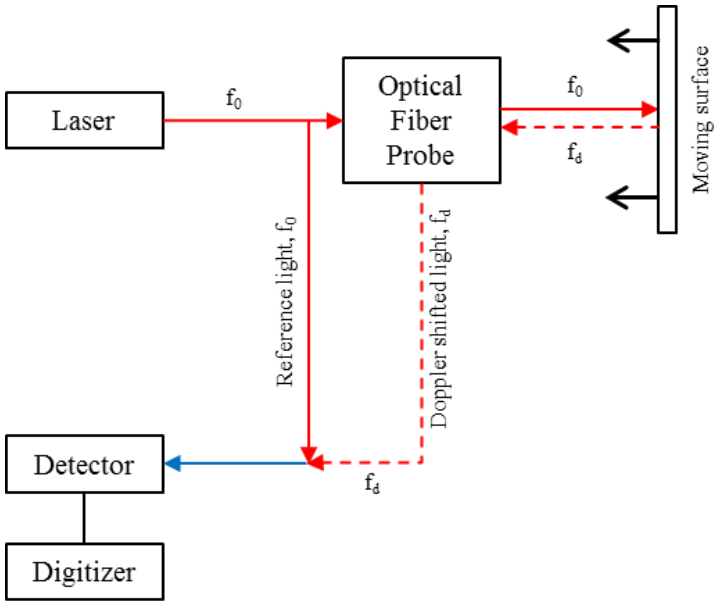

Figure 1.2 Overview of a PDV Measurement

Here, light at frequency f_0 interferes with light at f_d at the detector and is recorded by a digitizer. f_d is Doppler-shifted away from f_0 by the motion of the surface at right, so that one fringe corresponds to motion of the surface toward the probe of $\lambda/2$.

Advantages of PDV include its relative simplicity, robustness, cost, accuracy, and versatility [29]. Chau et al. [30] used PDV for shock Hugoniot measurements of a single-crystal copper plate during impact experiments.

Recently, PDV technology was used as a basis for developing MPDV, which employs frequency-domain and time-domain multiplexing with PDV. MPDV system records velocimetry data from multiple points onto a single digitizer channel. The concept of frequency upshift PDV or, heterodyne PDV (i.e. frequency-domain multiplexing) was first introduced by Daykin and Perez [31]. Daykin[32] proposed frequency-domain multiplexing using four channels into a single optical fiber and then multiplexed this previous configuration twice in the time domain to get eight

velocity histories in a single digitizer. Researchers are currently exploring the applications and abilities of MPDV systems [33–35]. Already, several new techniques are developed to analyze the large amount of data collected from MPDV systems [31,35].

Since impact studies of the plate perforation are conducted with expensive experimental devices and equipment, computational modeling and numerical simulation have become an acceptable way to investigate behavior of materials, with the goal of having a predictive capability for these kinds of impact events. Numerical solutions and computational modeling of plate perforation problems have been described by several researchers. Børvik, et al. used a constitutive material model of viscoplasticity with ductile damage in LS-DYNA to computationally simulate the perforation phenomena [36,37]. Chen et al. extensively studied plate perforation with different projectile nose shape; providing analytical and computational models to compare results [38–40]. Ductile spall fracture and post-spall behavior of a circular plate was simulated using the PRONTO finite element code [41]. Impact dynamics is a complex phenomenon and solution of computational model depends on selection of the proper physics models and input parameters [42]. High speed projectile impact on target generates an enormous amount of pressure and heat resulting in large deformation of both objects [43]. Recently, several computational packages based on hydrocode methods have been used for penetration modeling. Oblique impact of aluminum sphere on aluminum target plate was modeled in AUTODYN-3D hydrocode for an impact velocity of 6.5 km/s [44]. This code emphasized on the use of a proper erosion criteria. CTH hydrocode was used in multiple instances to model penetration problems [15,45–47]. Also, the Lagrangian based smoothed particle hydrodynamics (SPH) method is gaining popularity to simulate impact penetration problems [48–51]. Some of the work focused on modeling the

behavior of ceramic tiles under hypervelocity impact but they also included useful experimental data and computational material model properties for the metallic materials.

1.2 Research Objective

Literature reviewed so far mostly presented complete penetration of target plates rather than focusing on plastic deformation of plates in hypervelocity conditions. Therefore, one of the major objectives of this work is to design hypervelocity impact experiments where plastic deformation of metallic plates can be better understood.

Another key objective of this research is to explore the capability of newly developed MPDV system in hypervelocity impact events. Exploring the ability of MPDV system will certainly give direction to resolve some of the existing issues in this type of experiments and may have potential to challenge traditional diagnostic system.

One of the major challenges of this work is to verify the experimental data collected from the MPDV system. Therefore, developing simulation models with available resources which can predict experimental results accurately enough is selected as another objective of this work.

To achieve all of these objectives, the work has been divided into few subgroups:

1. Design of a simple plate penetration experiment with gas gun which can capture plastic deformation of metallic plates.
2. Design of a data acquisition system.
3. Conduct series of dynamic impact experiments with different MPDV arrangements.
4. Qualitative measurement of target plates in post-shock experiment.

5. Analyze the extracted velocimetry data from MPDV system.
6. Develop simulation models using finite element analysis (FEA) packages to verify experimental data.

CHAPTER 2 EXPERIMENTAL SETUP

In all ballistic and hypervelocity events, structures experience wide range of shock loading- often as complex as mine blast to a simplistic one like projectile impact. Due to high impact energy of this type of loading, deformation and failure produced in these structures are often studied to understand the fundamental shock properties. All the plate impact experiments in UNLV has been performed using a two-stage light gas gun designed by Physics Applications Inc.. Designing of a gas gun and theory behind it, is beyond the scope of this work. This chapter, however, represents the working principle of two stage light gas gun, designing of plastic deformation experiments of metallic experiments using gas gun, designing of test fixture and diagnostic equipment required during the experiments.

2.1 UNLV Two-stage Light Gas Gun

UNLV gas gun has been designed to shot 0.22-caliber Lexan projectiles at a velocity up to 7 km/s. Main components of the gas gun with a schematic has been presented in Figure 2.1. As shown in the figure, main components of the gas gun includes powder chamber, pump tube, center breech, launch tube, blast tank, drift tank and target chamber. Pump tube of the gas gun is 1.49 m long and 19 mm in diameter. At the first step of gas gun operation, pump tube is filled with light gas like helium or hydrogen. Projectile velocity of the gas gun can be controlled in multiple ways: changing fill gas pressure in pump tube and amount of gun powder supposed to be most common techniques. Lighter gas is generally used to obtain for higher projectile velocity as velocity of the projectile is usually limited by the sound speed of the gas i.e. molecular weight of the gas.

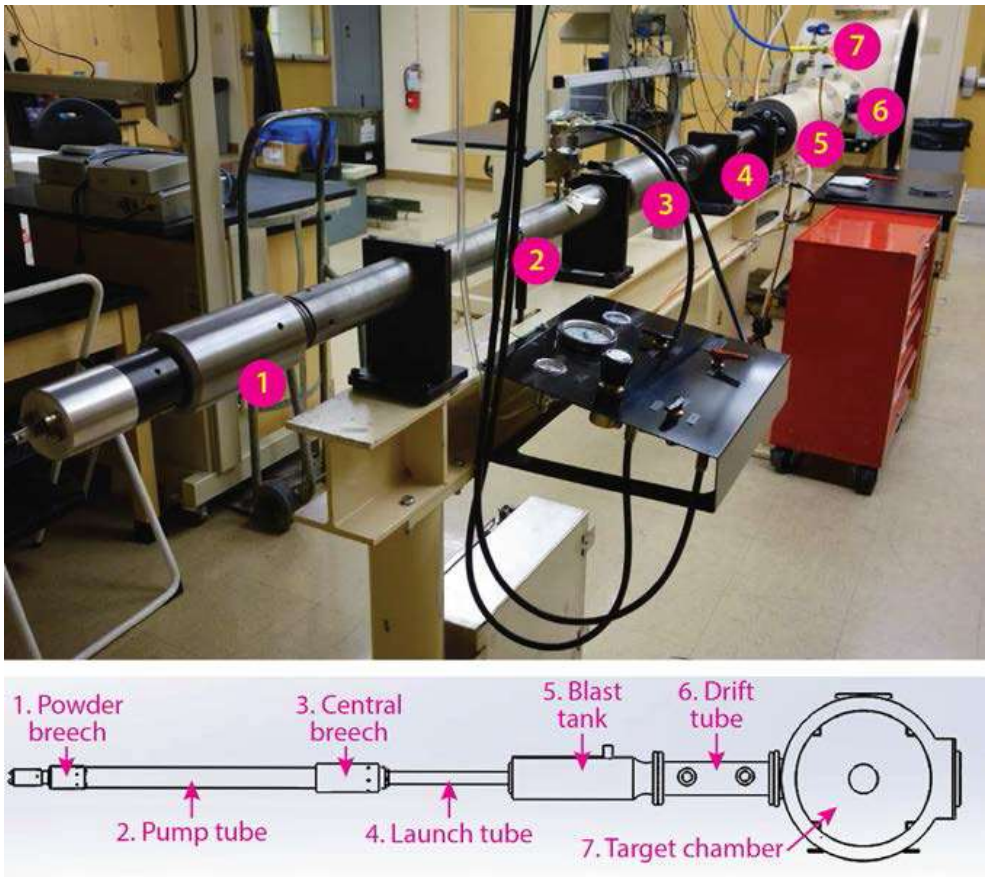

Figure 2.1 Two-stage Light Gas Gun at UNLV with Schematic

Typically, pump tube is sealed with a piston of 20 mm in diameter and 120 mm long (Figure 2.2) in one side. The piston, supplied by PAI, has an average weight of 26.8 gm for all the experiments conducted. Powder chamber (Section 2.1.1) is assembled to the pump tube before light gas filling on that side. A cap breech is also connected behind the powder chamber with a high voltage cable and a solenoid firing pin. On the other side, pump is connected with launch tube with a high pressure unit called 'central breech' assembly. The central breech has an opening of 20 mm diameter on pump tube side and 5 mm diameter opening on launch tube side. The 1.016 m long launch tube guides the projectile and constrains the pump gas as the projectile accelerates.

Figure 2.2 Piston

2.1.1 Powder Breech and Pump Tube

Powder chamber (Figure 2.3) contains a certain amount of gun powder which burns during the gas gun operation. This gun powder is ignited by firing of a primer at the back of a cartridge (Figure 2.4). The cartridge, also filled with gun powder, is placed to seal one opening of the powder chamber. The discharge of capacitor is used to activate a solenoid which drives a firing pin into the primer. The capacitor (Figure 2.5) in normally charged by AC power supply. The gun powder in the cartridge burns rapidly when struck by firing pin. This then ignites the gun powder in the powder chamber.

Figure 2.3 Powder Chamber

Figure 2.4 Cartridge

Figure 2.5 High Voltage Capacitor

Figure 2.6 Firing Panel

Figure 2.7 Cap Breech

The resulting explosion propelled a piston in the pump tube filled with pressurized helium gas. As the piston moved forward, it increased the pressure of the helium/ hydrogen gas in the pump tube. In most of the experiments in this work, pump tube was filled with helium gas of a certain pressure. Pump tube is evacuated completely before filling up propellant gas to ensure the consistency of gun dynamics. The gun powder used in powder chamber is IMR 4064 and green dot smokeless powder respectively. In this work, most of the time the amount of gun powder used is 20 gm and the amount of green dot powder in the cartridge is 0.6 gm.

2.1.2 Central Breech and Launch Tube

The central breech between the pump tube and launch tube is shown in Figure 2.8. During the experiment, the central breech unit stops the moving piston and ensures a high pressure gas flow at the base of projectile by rupturing a petal valve. The central breech assembly is one of the

most critical parts to check during gas gun operation which affects the gas gun performance [1]. As mentioned earlier, petal valve withstands the high pressure of gas until it reaches a break point and ensures a gas flow to accelerate the projectile. Figure 2.9, shows typical petal valve before and after experiment. Since this pressure is dynamic and not static, it's difficult to find actual pressure for the opening of the valve. The petal valve is placed on O-rings to avoid the leakage of gases from the central breech assembly.

Figure 2.8 Central Breech

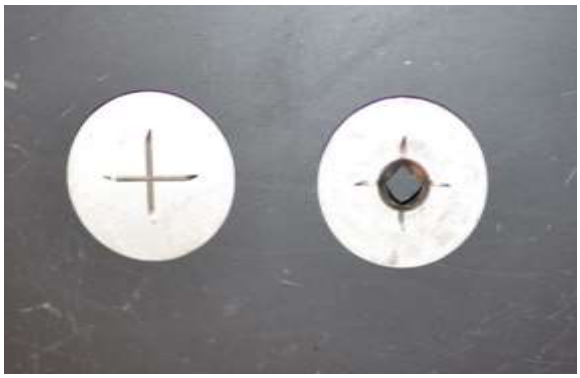

Figure 2.9 Petal Valve (Before and After Experiment)

The projectile used in all gas gun experiments was cylindrical lexan (i.e. polycarbonate) projectiles with a diameter of 5.58 mm and a length of 8.61 mm (Figure 2.10). Average weight of this lexan projectiles is 0.25 gm. Polycarbonate projectiles are generally used since it acts as a lubricating agent as it moves along the launch tube. Projectile is placed inside the rifled launch tube before the central breech assembly.

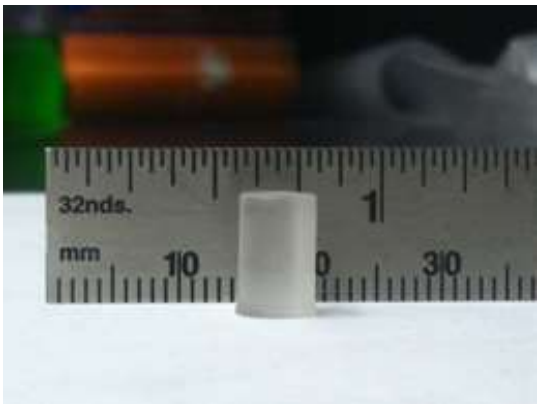

Figure 2.10 Lexan Projectile (0.22-caliber)

Figure 2.11 Launch Tube

2.1.3 Blast Tank, Drift Tube and Target Chamber

Figure 2.12 shows the blast tank which is approximately 0.228m in diameter and 0.812m in length provides the volume for the expansion of the propellant gas. Blast tank is connected to the drift tube (Figure 2.13) where projectile velocity is monitored by diagnostic instrument. Drift tube is 0.152m in diameter and 0.609m in length. Drift tube has two see through glass ports where laser beams are passed.

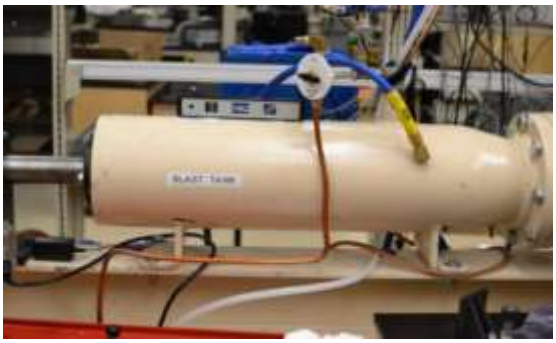

Figure 2.12 Blast Tank

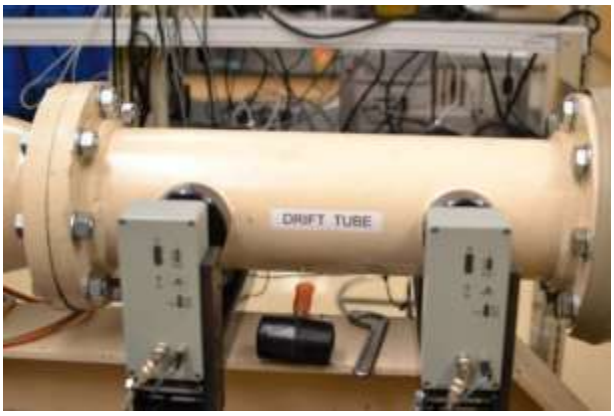

Figure 2.13 Drift Tube

The target chamber, as shown in Figure 2.14, is the final stage of the gas gun. It is 0.6096m in diameter and 0.3048m deep. The target tank provides space for mounting the bolted joint fixture and carry instrumentation. Ports in the target tank as shown in Figure 2.15 provide access for various instrumentations. All flanges, ports and joints in the tank assembly are assembled together with O-rings. This is done to isolate the interior volume from the atmosphere.

Figure 2.14 Target Chamber with Mounting Plate Inside

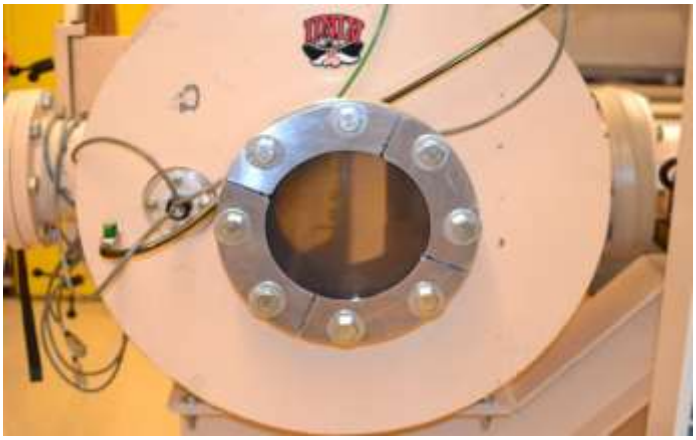

Figure 2.15 Ports for Instrumentation

During the gas gun operation, after placing the target in the target chamber and diagnostic instruments inside, target chamber is closed. Launch tube, central breech, pump tube and powder breech are assembled together. The whole assembly is then evacuated to a vacuum level of around 4 Torr (0.0053 atm) before filling pump tube with light gas. Once the vacuum level is reached, pump tube is filled with hydrogen/helium gas, powder chamber is loaded with gun powder and placed on the pump tube. A cartridge is then installed in the powder bridge, and cap breech is assembled in the powder chamber and firing cable is attached. After that, vacuum pump is turned off, and all the diagnostic instruments are rechecked. Firing pin is placed inside the cap breech and the gas gun is fired from the firing unit section.

2.2 Diagnostics

2.2.1 Projectile Velocity Measurement

During gas gun operation, it is very important to measure the projectile velocity as the basic gun dynamics, performance can be understood from it. In UNLV gas gun, projectile velocity is measured by using a two station laser intervalometer system. The unit has two collimated laser sources at 0.3048 m apart (Figure 2.16). Each laser beam is passed through one port to a receiving station. These collimated laser line generator are used to illuminate a linear array of 32 photodiodes. The passage of an object is sensed by the reduction of light level at one or more of the photodiodes. The diode array is covered with a narrow bandpass filter centered on the 670 nm wavelength of the laser so as to reduce interference from stray light. The diode array spans a length of 0.0508 m (2 inch). There is a timer unit which is a six-digit counter enabled by an external START pulse and disabled until receives an STOP signal. During gas gun operation, ‘start’ pulse

is triggered by the projectile when interferes the first laser unit source. Once the projectile crosses the second laser unit source, the timer receives a ‘stop’ signal and displays the time difference of projectile movement in between two laser sources. As the distance is known between the laser sources, the projectile velocity can be calculated based on the timer value (Figure 2.17).

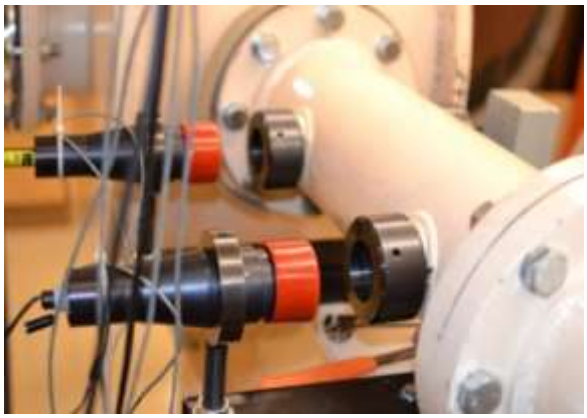

Figure 2.16 Laser Unit Assembly

Figure 2.17 Timer Unit of Intervalometer System

2.2.2 Gas Handling System

The gas handling unit (Figure 2.18) is one of the major components for gas gun operation. It is used for multiple operations: evacuation of gas gun, fill up and vent out gas in pump tube. The control panel in gas handling unit has two pressure gauges that monitors the pressure of the gas cylinder and pump tube. Hydrogen/Helium gas cylinders are connected with the gas handling unit with high pressure pump tube hoses. In order to fill up hydrogen/helium gas in the pump tube, a manually operated valve is used. The vacuum pump is also connected with the gas handling unit system. A regulator is used to handle the pressure and vacuum in the system. Besides this, a vent valve is present in this gas control panel which can be used to evacuate the system after experiment or, during emergency.

Figure 2.18 Gas Handling Unit

2.2.3 MPDV

The architecture of MPDV system is already explained by E. Daykin [31]. A schematic view of this architecture is presented on Figure 2.19. The architecture utilizes four laser pairs with different wavelength; each pair consists of a laser used for measurement and another for reference. The laser frequencies correspond to separate ITU bands allowing for the use of commercial dense wavelength division multiplexing (DWDM) modules that passively combine multiple lasers of different frequency onto a single fiber. This combined (multiplexed) signal passes through the input leg of a 3-port optical circulator and then into a demultiplexer (DeMux) where the frequencies separate onto individual fibers. The measurement lasers launch through lens packages onto the target, reflect back, and re-enter the same launch fiber. Once the light exits the circulator, a simple erbium-doped fiber amplifier (EDFA) amplifies the measured power levels. An additional stage of Mux/DeMux allows for individual attenuation to balance optical powers. A high bandwidth oscilloscope and photo-detector (P-D) record the four "beat" frequencies exiting the 1x2 coupler produced when the measurement lasers mix with their respective reference lasers.

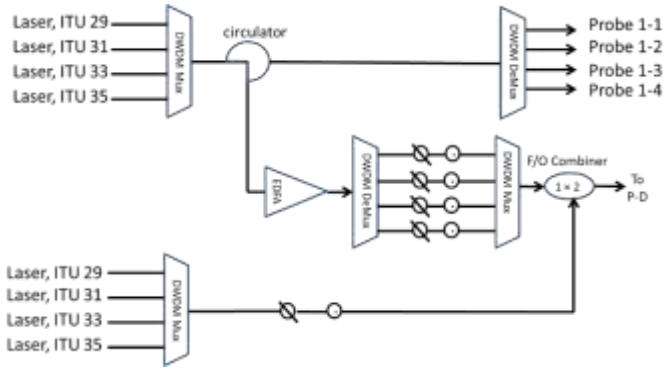

Figure 2.19 Schematic of MPDV Architecture

Figure 2.20 Typical MPDV Architecture

2.3 Materials

Three different types of materials were used in this work: A36 steel, 304L and HY100. The primary purpose of this work was to measure the plastic deformation of A36 steel plates in hypervelocity conditions. This study initially started to explore A36 steel behavior but due to lack of adequate information on the pressure-induced phase transition of A36 steel; the study was expanded to two other well characterized steels: one with pressure-induced phase transition (HY100) and another without any pressure-induced phase transition (304L). Details of those plates are given below. All of these materials were supplied by NSTec. Typical chemical composition and mechanical properties of these materials are listed in Table 2.1 and 2.2.

Table 2.1 Typical Chemical Composition (%) †

Material	A36	304L	HY100
Iron, Fe	98.00	71.629	95.300
Nickel, Ni	0.060	8.021	2.470
Chromium, Cr	0.070	18.075	1.240
Manganese, Mn	0.430	1.724	0.310
Carbon, C	0.200	0.021	0.160
Copper, Cu	0.180	0.000	0.080
Molybdenum, Mo	0.012	0.293	0.250
Silicon, Si	0.080	0.204	0.210
Phosphorous, P	0.012	0.032	0.005
Vanadium, V	0.002	0.000	0.004
Sulfur, S	0.005	0.001	0.001
Titanium, Ti	0.001	0.000	0.001

† As received material datasheet supplied by NSTec

Table 2.2 Typical Physical and Mechanical Properties [††]

Property	A36	304L	HY100
Density (kg/m^3)	7890	8000	7900
Tensile Strength, Ultimate (MPa)	455	653.1	789.4
Tensile Strength, Yield (MPa)	345	427.7	706.7
Young's Modulus (GPa)	200	200	207
Bulk Modulus (GPa)	140	167	172
% Elongation at Break (in 50 mm)	28.0	45.4	32.0
Poisson's ratio	0.26	0.30	0.28

†† As received material datasheet supplied by NSTec

2.4 Experimental Setup for Plastic Deformation Experiments

2.4.1 Target Plates

All metallic plates were cut with a dimension of 0.1524 × 0.1524 × 0.0127 m (6"× 6 × 0.5"). The thickness of the target plates was chosen such that during gas gun experiments projectiles can't penetrate the plates completely; instead produce a bulge on the bulge. Target plates had four 5½" holes. Figure 2.21 shows a schematic of the target plate dimensions in gas gun experiments.

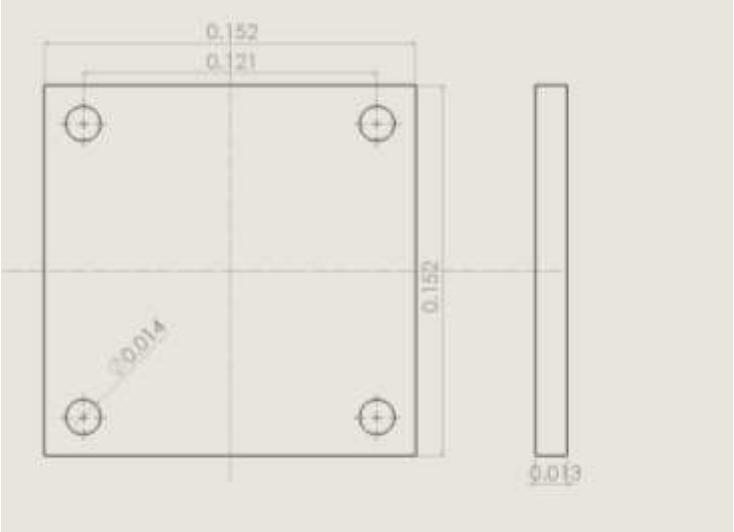

Figure 2.21 Schematic of Target Plates in Gas Gun Experiments (Dimensions in m)

Typically, MPDV optical probes were focused on the back side of the target plates placed in the test chamber to collect velocimetry data. A small surface area of target plates was prepared for MPDV data collection. Target plates were prepared by using grinder, sand paper and finally a ball roller. The surface of the target plates was prepared such that all the lasers from the MPDV optical fibers diffracted uniformly instead of a complete reflection. This ensured a certain return signal to the MPDV recording system during experiment. Figure 2.22 shows an unprepared and prepared A36 target plate.

(a) Typical Unprepared Target Surface

(b) Typical Prepared Target Surface

Figure 2.22 Typical Target Plates for MPDV System

2.4.2 Target Holder

Target holder was designed to hold the target plates in the test chamber. It was made of A36 steel. As mentioned earlier, targets were bolted with this target holder. The schematic dimension of target holder is presented in the Figure 2.23 and an exploded view of target and target holder assembly in Figure 2.24.

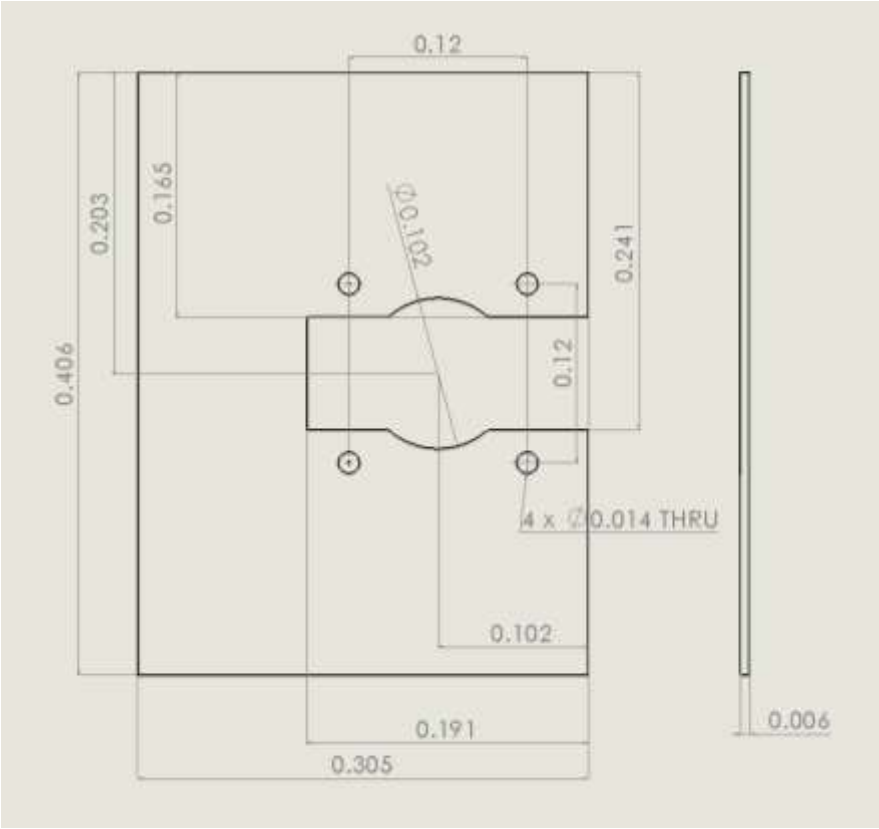

Figure 2.23 Schematic of Target Holder (Dimensions in m)

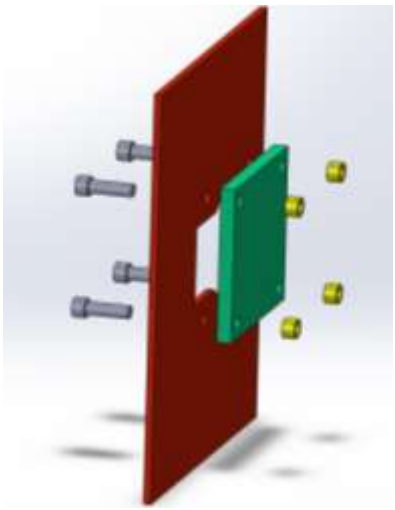

Figure 2.24 Exploded View of Target, Target Holder and Bolts

The target holder was fixed to two ¼" thick optical bread boards (top and bottom) through four angle brackets. The optical bread boards and angle bracket assembly were shown in Figure 2.25.

Figure 2.25 Target Holder Support System

2.5 Experiment

All plastic deformation experiments in gas gun were performed with Helium gas. In all experiments, lexan projectiles impacted target plates. Projectiles achieved a velocity of 4.5 km/s-7.0 km/s. Typical flowchart of a gas gun experiment is presented in Figure 2.26.

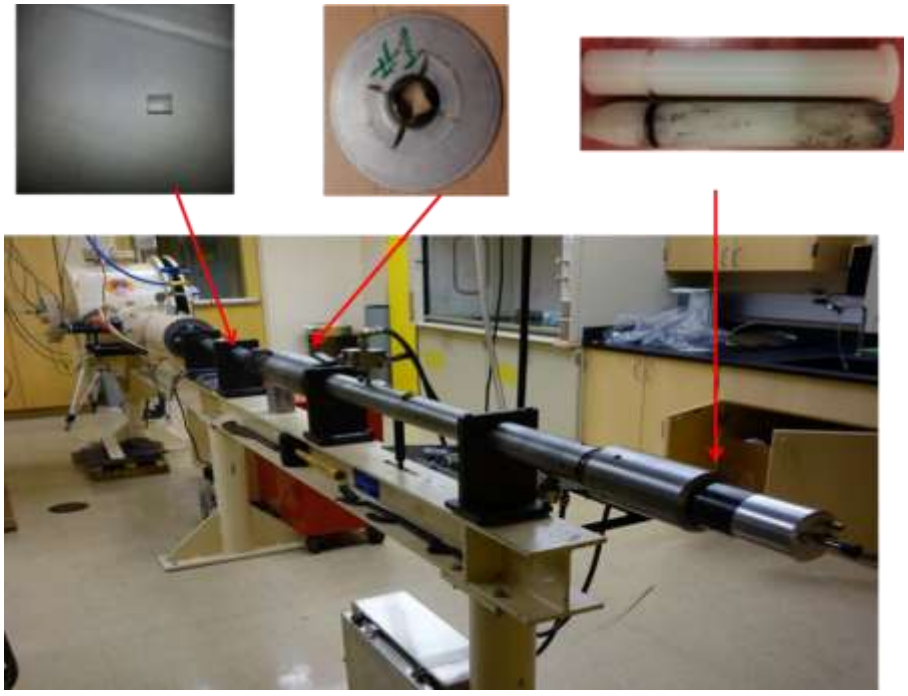

Figure 2.26 Flowchart of Gas Gun Operation

Velocimetry data were collected by the MPDV system with the optical fiber probes placed inside the chamber focusing on the back side of the target plate. When the projectile crossed the 'START' laser, the intervalometer and MPDV system were triggered simultaneously by the signal. Two delay generators, showed in Figure 2.27, were used to set a delay time of 70-110 μs typically depending on the projectile velocity. The reason for setting a delay was to ensure that the

oscilloscope used in the MPDV system collects the velocimetry data effectively without missing any actual shockwave phenomena from the backside of the target plates. Data were captured by two 4-channel Tektronix oscilloscopes as frequency spectrogram (Figure 2.28). These oscilloscopes had a bandwidth of 6 GHz and a sample rate of 2×10^9 Sample/s in 2-channel mode and 10^9 Sample/s in 4-channel mode. MPDV instruments were fielded by NSTec operators. This recorded data were then collected by NSTec personnel on-site for further analysis. Velocimetry data were extracted by the performing a sliding Fourier analysis by NSTec personnel with their software and finally, provided as time vs. velocity for each individual experiment.

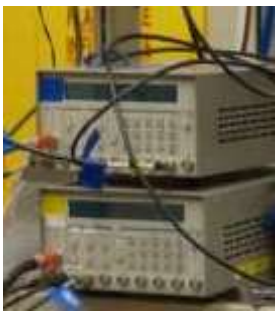

Figure 2.27 Delay Generator

Figure 2.28 Typical Tektronix Oscilloscope

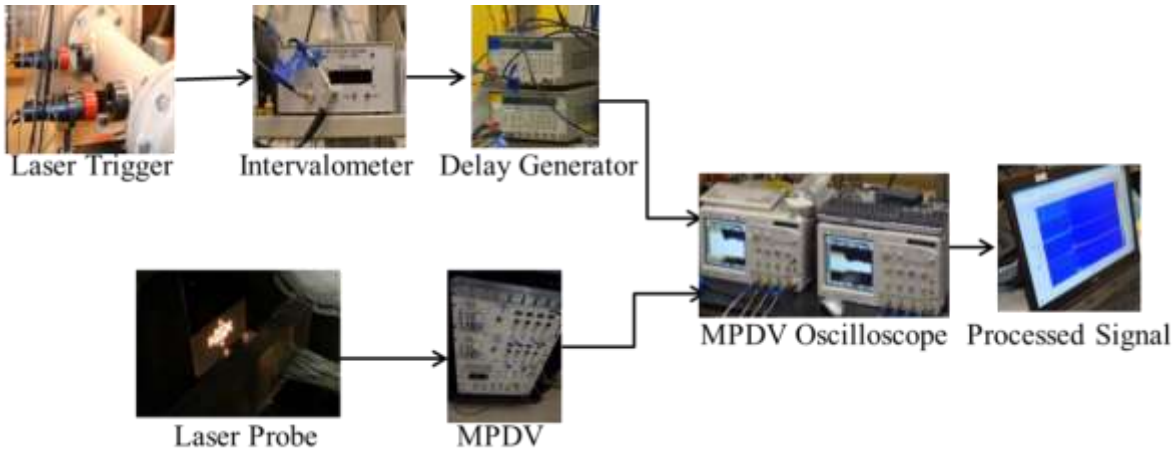

Figure 2.29 Typical Flowchart of Data Collected by MPDV Setup in Experiment

2.6 Test Matrix

Based on the MPDV probes arrangement, a number of experiments were conducted to monitor the plastic deformation. Schematic of typical probe arrangements are presented in Figure 2.30 and actual probe arrays in Figure 2.31. Distance and location of probes are listed in Table 2.3.

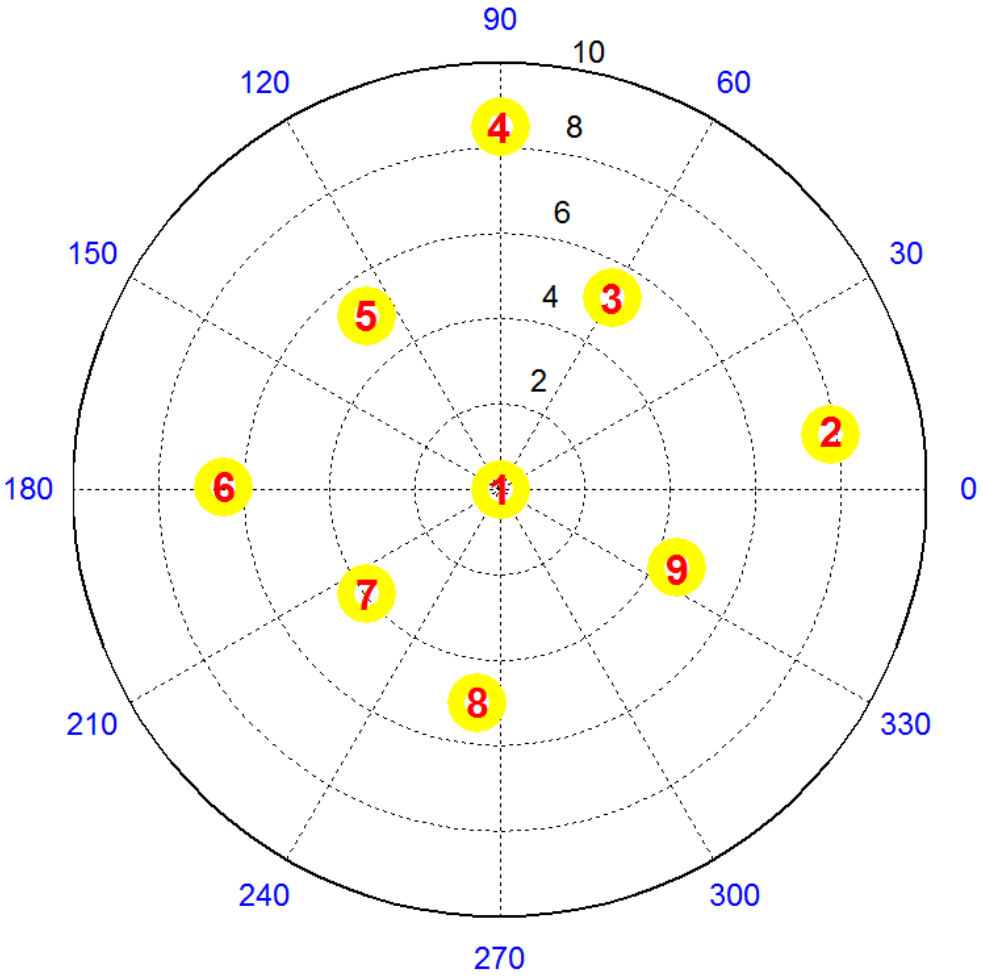

(a) Typical 9-probe MPDV Array

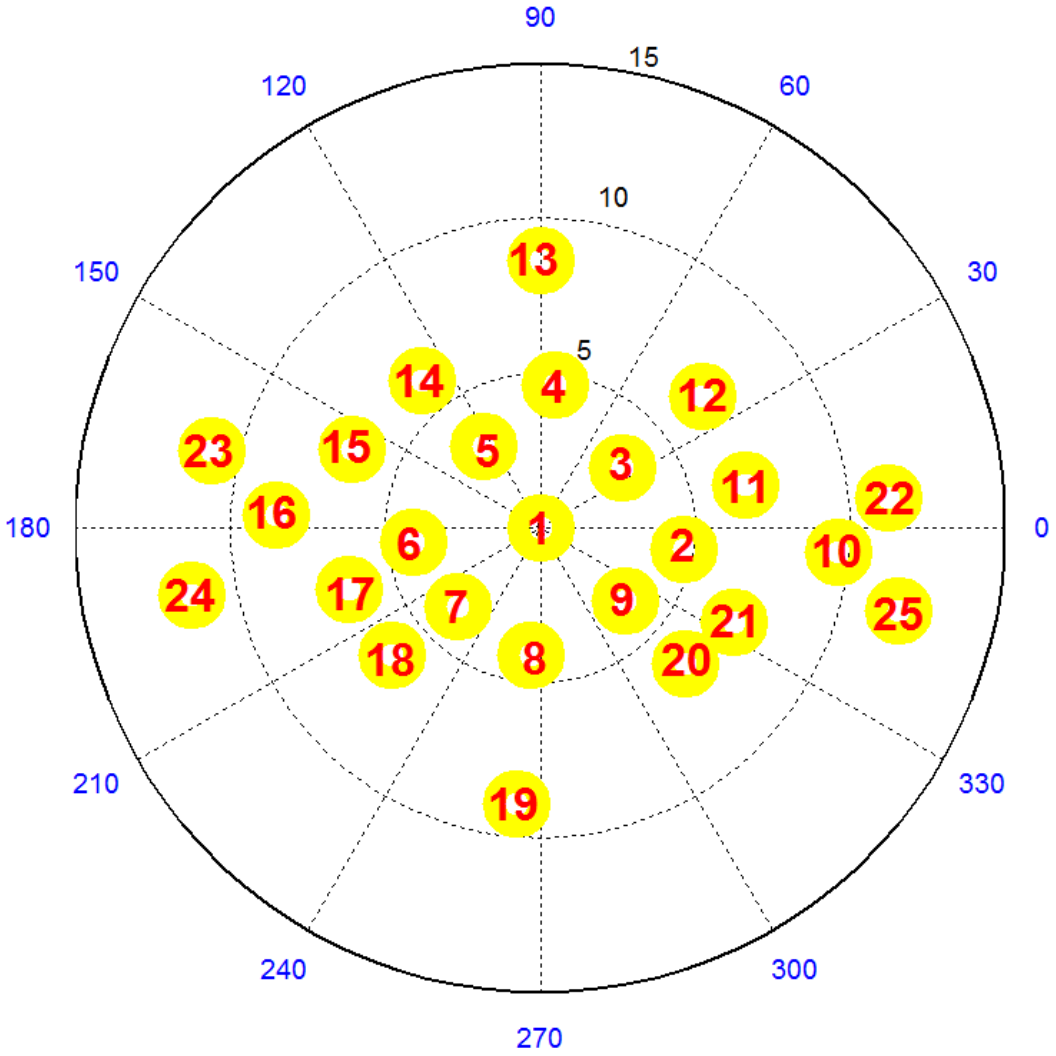

(b) Typical 25-probe MPDV Array

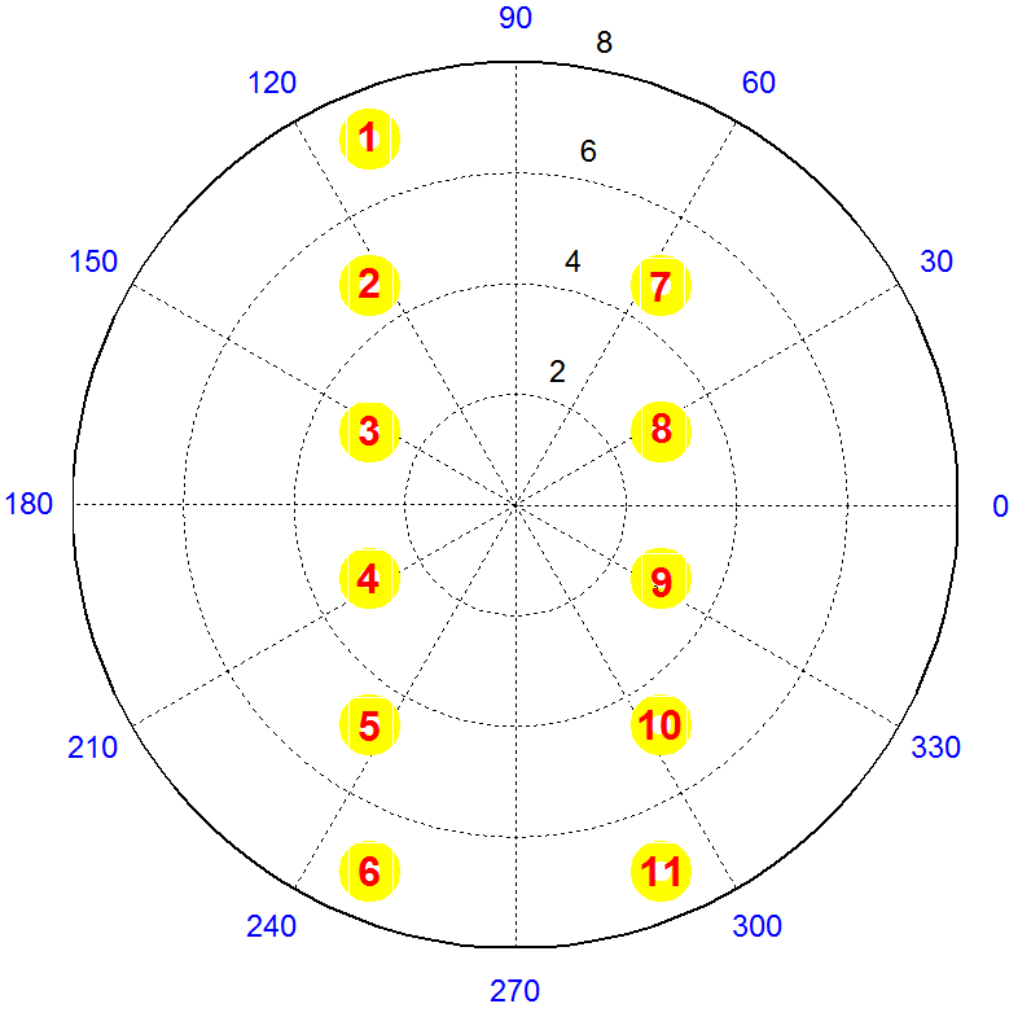

(c) Typical 11-probe MPDV Array

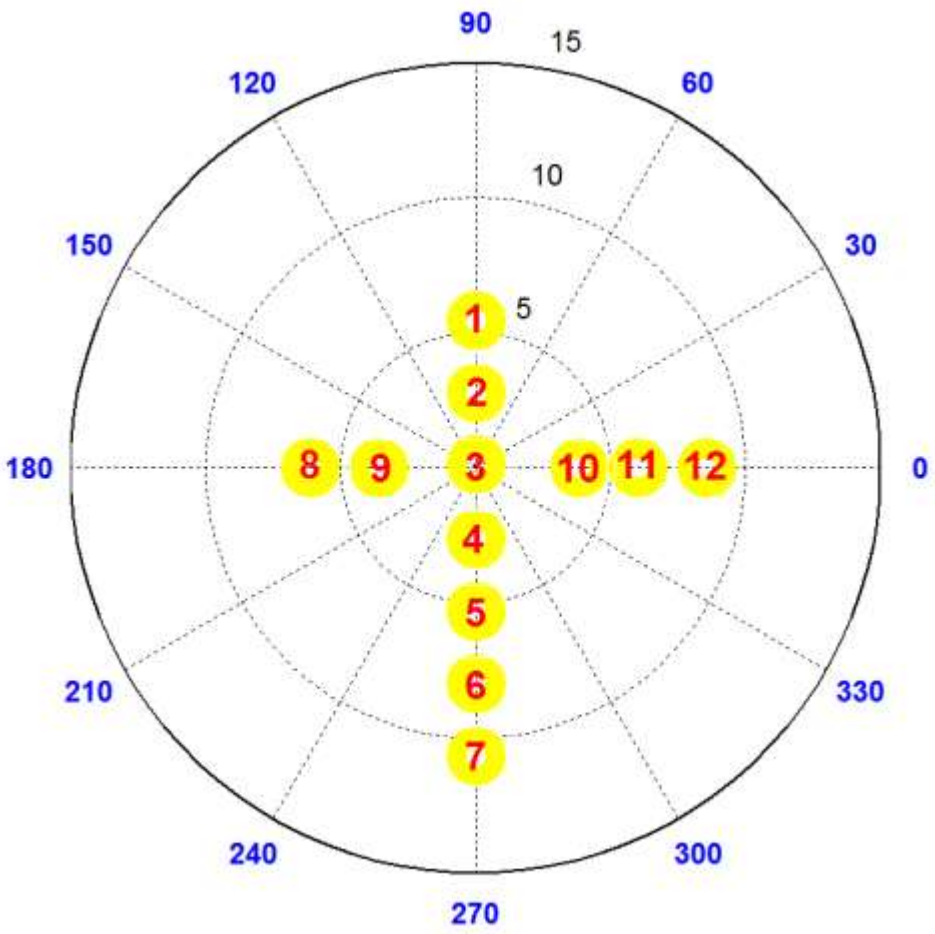

(d) Typical 12-probe MPDV Array

Figure 2.30 Schematic of MPDV Probe Arrangements.

In all pictures, ‘Black’ fonts represent radial distance of probes in mm, ‘Blue’ fonts are angular distance of probes in Degree, ‘Yellow’ markers represent the probes and ‘Red’ fonts represent the corresponding probe identity in MPDV setup.

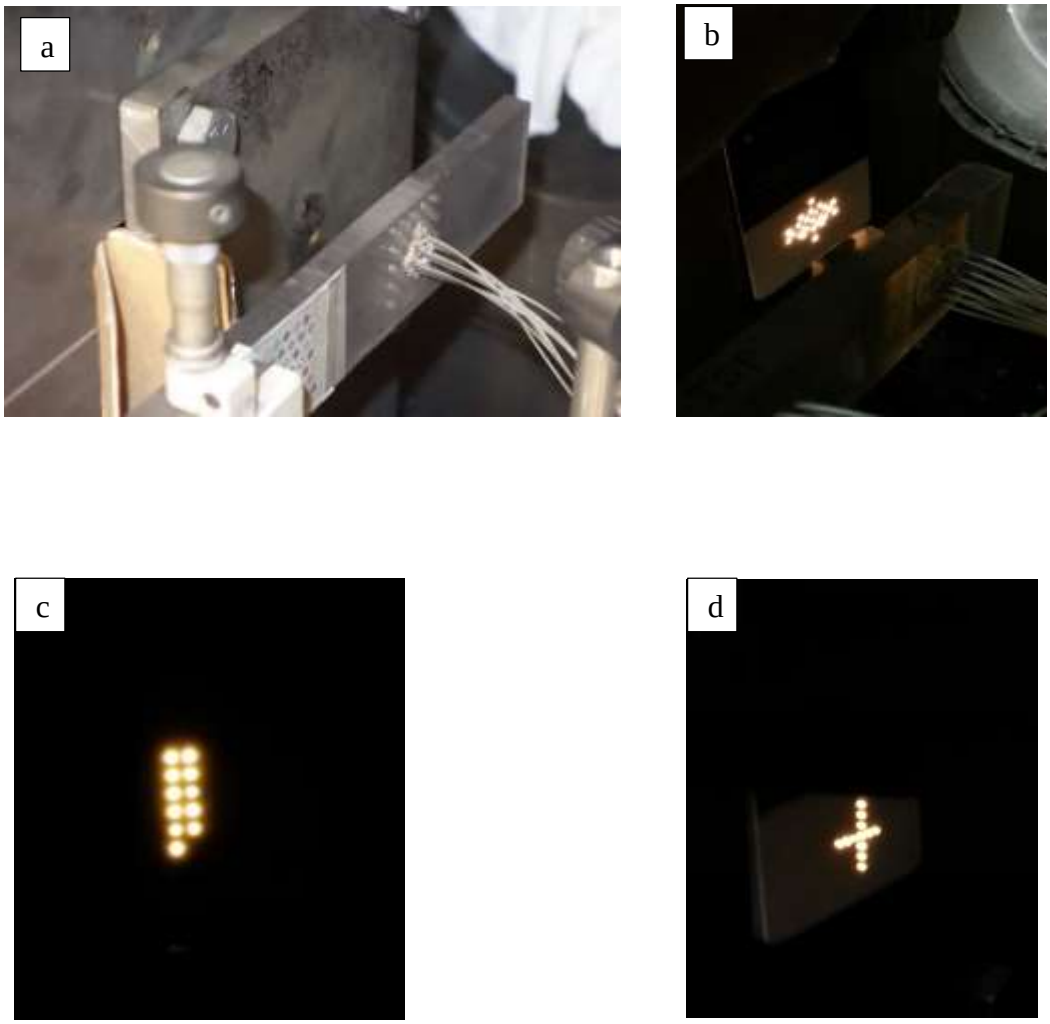

Figure 2.31 Typical MPDV Probe Arrangements on the Back Side of Target Plates in Experiments: (a) 9-probe (b) 25-probe (c) 11-probe (d) 12-probe

Table 2.3 Typical MPDV Probe Locations from Probe # 1 in 9-probe Experiment

Probe #	1	2	3	4	5	6	7	8	9
r , mm	0.00	7.85	5.21	8.50	5.11	6.48	3.96	5.02	4.52
θ, deg	0.00	9.40	59.60	89.90	127.50	179.50	218.00	263.80	336.40

Table 2.4 Typical MPDV Probe Locations from Probe # 1 in 25-probe Experiment

Probe #	*1*	*2*	*3*	*4*	*5*	*6*	*7*	*8*	*9*
r , mm	0.00	4.69	3.31	4.64	3.17	4.12	3.69	4.13	3.62
θ, deg	0.00	351.42	36.04	83.81	124.59	186.13	224.01	265.70	319.59
Probe #	*10*	*11*	*12*	*13*	*14*	*15*	*16*	*17*	*18*
r , mm	9.68	6.77	6.75	8.63	6.10	6.60	8.53	6.48	6.30
θ, deg	355.31	11.84	38.81	89.73	128.75	157.47	177.18	197.83	220.95
Probe #	*19*	*20*	*21*	*22*	*23*	*24*	*25*		
r , mm	8.93	6.40	6.95	11.28	10.89	11.47	11.87		
θ, deg	265.11	316.77	334.10	4.98	166.78	190.95	346.95		

Table 2.5 Typical MPDV Probe Locations from Probe # 1 in 11-probe Experiment

Probe #	*1*	*2*	*3*	*4*	*5*	*6*	*7*	*8*	*9*
r , mm	7.14	4.78	2.96	2.96	4.78	7.14	4.78	2.96	2.96
θ, deg	111.74	123.62	153.43	206.57	236.38	248.26	56.38	26.57	333.43
Probe #	*10*	*11*							
r , mm	4.78	7.14							
θ, deg	303.62	291.74							

Table 2.6 Typical MPDV Probe Locations from Probe # 1 in 12-probe Experiment

Probe #	*1*	*2*	*3*	*4*	*5*	*6*	*7*	*8*	*9*
r , mm	5.46	2.77	0.14	2.64	5.29	7.98	10.67	6.12	3.59
θ, deg	90	90	90	270	270	270	270	180	180
Probe #	*10*	*11*	*12*						
r , mm	3.86	6.05	8.57						
θ, deg	0	0	0						

Different MPDV probe arrangements were tried in different gas gun experiments to monitor the quality of the velocimetry data and comparing the performance of that MPDV setup. Furthermore, test matrices were developed to explore plastic deformation of different materials. Table 2.7 lists all the experiments planned for each material.

Table 2.7 Test Matrix

Materials	MPDV System Details	Number of shots planned in different impact velocity		
		< 5.0 km/s	5.0-6.0 km/s	> 6.0 km/s
A36	9-probe	1	1	-
	25-probe	1	2	-
304 L	11-probe	-	-	1
	12-probe	-	-	1
HY 100	11-probe	-	-	1
	12-probe	-	-	1

2.7 Typical Experimental Results

2.7.1 Physical Observation

In all gas gun experiments, impact of high-velocity Lexan projectiles created a crater on the front side and a bulge on the back side of target plates (Figure 2.32). Lexan projectiles disintegrated due to the enormous pressure and heat generated upon impact. After each experiment, crater and bulge details for each target plate were measured. The distance between the flat rear

surface of the plate and peak point of the bulge was taken to be the height of the bulge. An average value for multiple measurements of crater diameter, depth of penetration and bulge were taken as the final measurement.

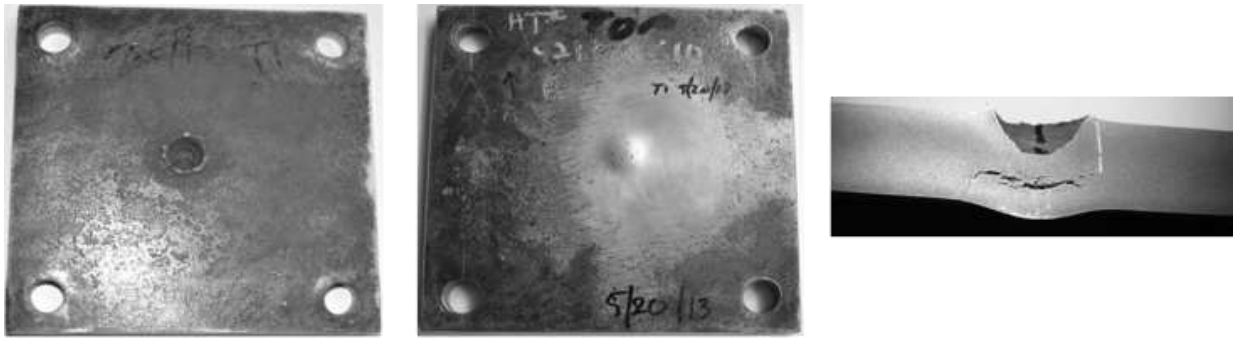

Figure 2.32 Typical Target Plate After Impact (Impact Velocity 4.763 km/s)

All the crater details and bulge dimensions are listed in Table 2.5. Sectioned plates showed spall due to release wave interactions. The results show that the size of spall cracks is proportional to impact velocity. Details of spall cracks from some of these experiments are also listed in Table 2.8.

Table 2.8 Physical Measurement of Target Plates after Impact

MPDV system details	Target Plates	Impact velocity, km/s	Crater diameter, mm	Penetration depth, mm	Bulge, mm	Spall crack details	
						Diameter, mm	Width, mm
9 probe	A36	4.763	15.4 ± 0.3	6.5 ± 0.3	1.4 ± 0.1	14.5 ± 0.2	0.2 ± 0.1
		5.708	17.2 ± 0.3	7.7 ± 0.3	3.1 ± 0.3	21.4 ± 0.2	1.9 ± 0.1
11 probe	304L	6.583	17.3 ± 0.2	6.4 ± 0.3	2.4 ± 0.1	13.6 ± 0.2	0.6 ± 0.1
	HY100	6.698	16.5 ± 0.3	6.4 ± 0.2	3.0 ± 0.3	14.6 ± 0.1	1.6 ± 0.4
12 probe	HY100	6.743	15.5 ± 0.1	4.5 ± 0.3	3.3 ± 0.1	14.1 ± 0.1	0.7 ± 0.2
	304L	6.758	15.5 ± 0.2	3.9 ± 0.1	3.2 ± 0.2	13.6 ± 0.2	2.2 ± 0.1
25 probe	A36	4.823	15.1 ± 0.2	6.5 ± 0.5	1.5 ± 0.1	14.8 ± 0.1	0.2 ± 0.1
		5.088	16.9 ± 0.8	7.0 ± 0.4	2.3 ± 0.2	n/a[†]	n/a[†]
		5.157	15.9 ± 0.4	6.5 ± 0.5	1.7 ± 0.2	18.5 ± 0.1	0.7 ± 0.1

[†]n/a – data was not available as the plate was not stored after impact

2.7.2 Free Surface Velocity

Typically, all MPDV experiments captured free surface velocities from target plate for 30-40μs whereas, the first 5μs contains the most important features related to the dynamic properties of the materials used. A typical free surface velocity from A36 steel experiment with a single probe is presented in Figure 2.33.

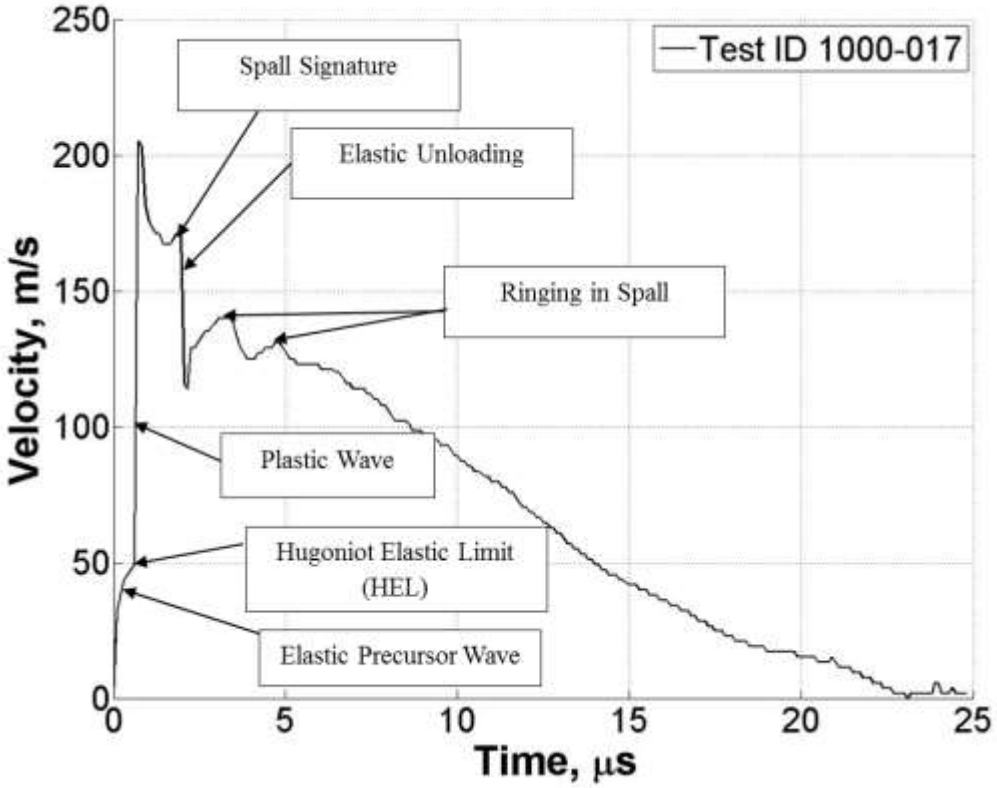

Figure 2.33 Characteristic Features of Typical Free Surface Velocity Profiles

In general, all free surface velocity profiles for A36 steel exhibited a two-wave structure velocity profiles in compression: an elastic wave followed by a relatively sharp plastic wave.

Velocity profiles also showed a second velocity peak and a spall signature in the form of a 'pullback velocity' signal. Free surface velocity profiles from 9-probe and 25 probes are shown in Figure 2.34 and Figure 2.35. Velocity profiles of 304L steel were pretty similar to A36 steel showing a two-wave structure with a sharp plastic rise (Figure 2.36). Because of known material properties differences between plain carbon steel (i.e. A36) and stainless steel (i.e. 304L), subtle differences do exist in the measured wave profiles. The velocity peak for the plastic wave was proportional to the impact velocity.

Supposedly, all low carbon alloy steels should show another wave rise after the plastic wave due to the $\alpha \leftrightarrow \varepsilon$ phase transition [13] similar to what was observed in shocked iron [14, 15]. However, in the case of HY100 steel, the signature of $\alpha \leftrightarrow \varepsilon$ phase transition was not prominent in 11-probe (Figure 2.37) and 12-probe gas gun experiments at the rear surface. This could be due to the complex, asymmetric nature of the stress wave at that location in the target plate, and the relatively low stress amplitude of the wave at the rear surface of the target plate. Typical fundamental shock compression experiments that do observe the phase transition wave have all been done with a condition of uniaxial strain, which was not the case for the stress wave in these MPDV experiments.

In all MPDV experiments, the impact center is within ± 3.0 mm from the nearest PDV probe. Therefore, probes located closest to the impact center showed the earliest arrival of the free surface velocity signal and showed the highest peak velocities in general; but there were certain exceptions. While the exact reason of these anomalies is not yet understood completely, possible reasons may include the complex asymmetric nature of the stress wave.

Tables 2.9-2.12 lists all the probe distances from impact center. Plate center was considered as datum i.e. (0,0) and radial distance of impact center from probe center was calculated initially. Details of calculating the impact center distance is discussed in APPENDIX B and C.

Table 2.9 Radial Distances of Probes from Impact Center in 9-probe Experiment (in mm)

	Impact Velocity, m/s	
	5708	4763
Impact center distance from plate center	7.70	5.47
Probe 1	2.41	0.74
Probe 2	5.52	7.97
Probe 3	4.60	5.84
Probe 4	8.92	9.24
Probe 5	6.90	5.74
Probe 6	8.88	6.57
Probe 7	5.99	3.59
Probe 8	5.71	4.29
Probe 9	2.44	4.24

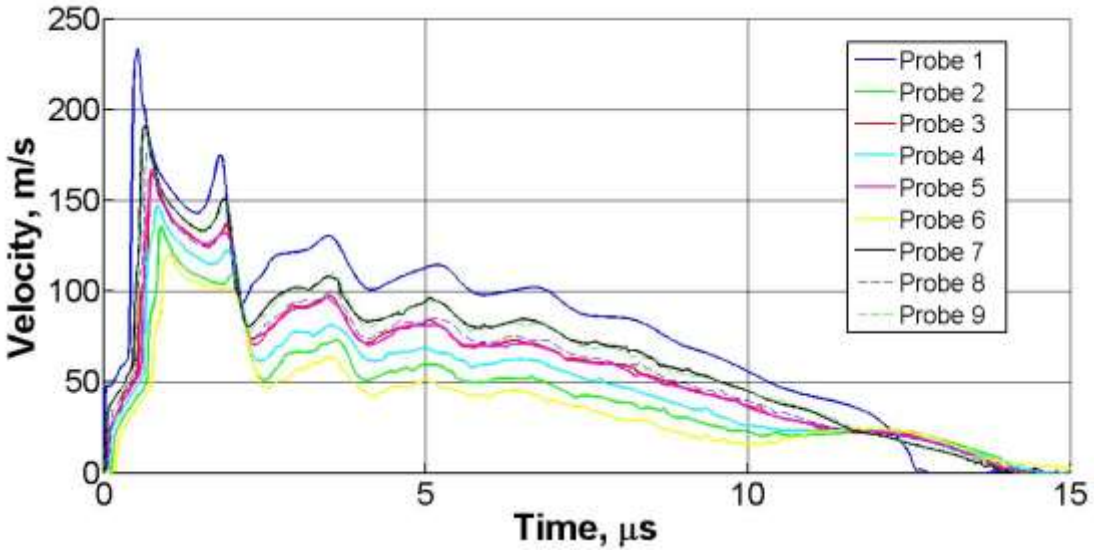

(a) 9-probe MPDV Experiment (Impact velocity: 4.763 km/s)

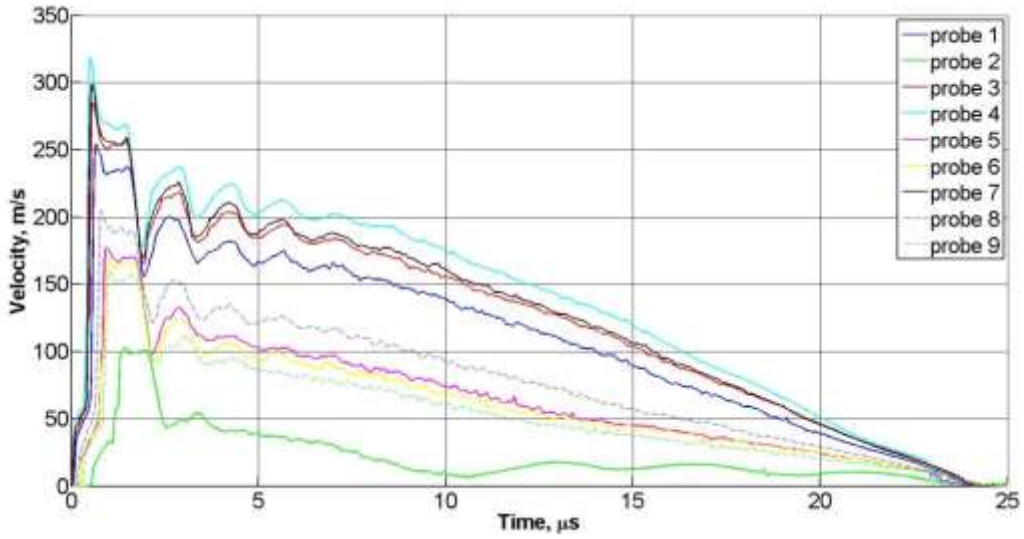

(b) 9-probe MPDV Experiment (Impact velocity: 5.708 km/s)

Figure 2.34 Typical Free Surface Velocity Profiles of A36 Steel with 9-probe MPDV Arrangement.

Table 2.10 Radial Distances of Probes from Impact Center in 25-probe Experiment (in mm)

	Impact Velocity, m/s		
	4823	5088	5157
Impact center distance from plate center, mm	5.18	3.62	7.81
Probe 1	0.82	1.08	2.24
Probe 2	4.44	5.75	2.68
Probe 3	3.70	3.99	1.62
Probe 4	5.42	4.47	4.54
Probe 5	3.96	2.35	4.57
Probe 6	4.31	3.21	6.35
Probe 7	3.36	3.39	5.68
Probe 8	3.36	4.57	5.17
Probe 9	2.99	4.66	2.80
Probe 10	9.68	10.71	7.54
Probe 11	6.79	7.69	4.54
Probe 12	7.14	7.34	4.91
Probe 13	9.43	8.29	8.51
Probe 14	6.86	5.19	7.43
Probe 15	7.12	5.52	8.56
Probe 16	8.80	7.52	10.72
Probe 17	6.48	5.69	8.70
Probe 18	5.98	5.89	8.31
Probe 19	8.15	9.30	9.75
Probe 20	5.73	7.42	5.38
Probe 21	6.45	8.03	5.32
Probe 22	11.48	12.25	9.06
Probe 23	11.29	9.83	12.97
Probe 24	11.55	10.58	13.71
Probe 25	11.51	12.93	9.85

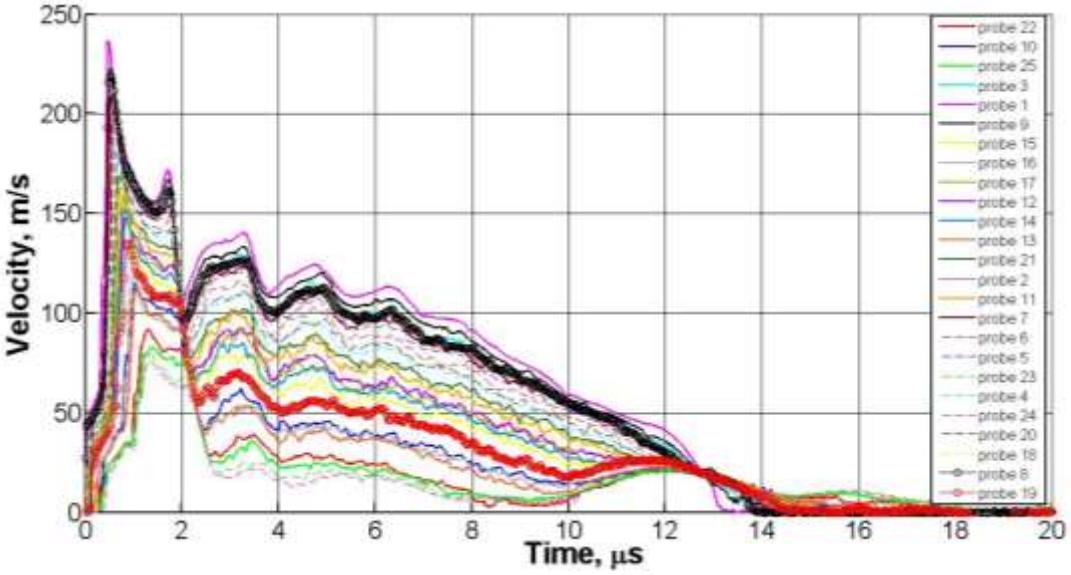

(a) 25-probe MPDV Experiment (Impact Velocity: 4.823 km/s)

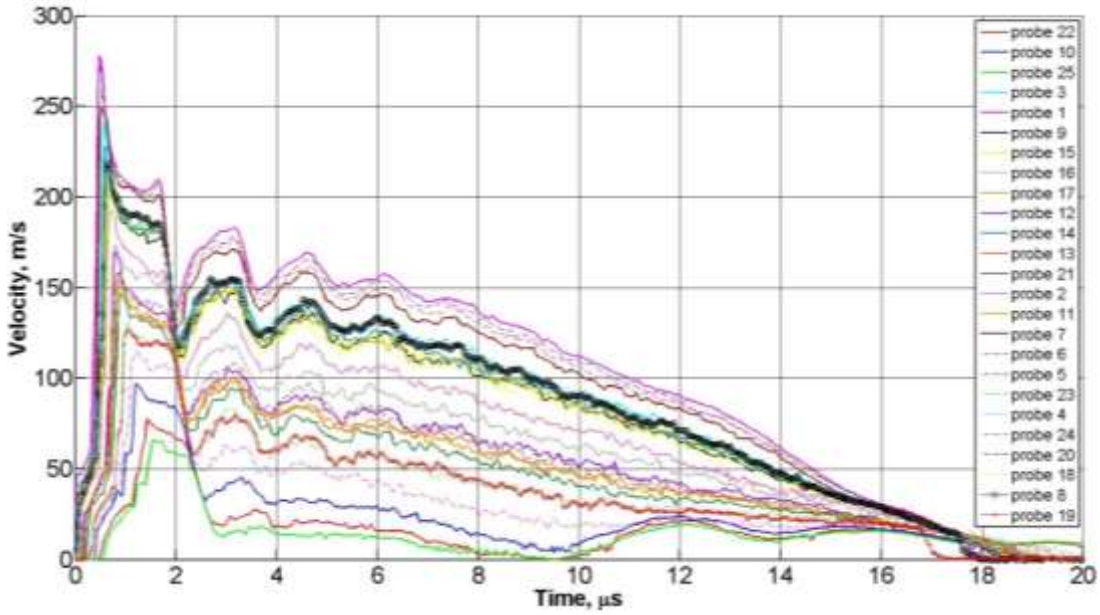

(b) 25-probe MPDV Experiment (Impact Velocity: 5.088 km/s)

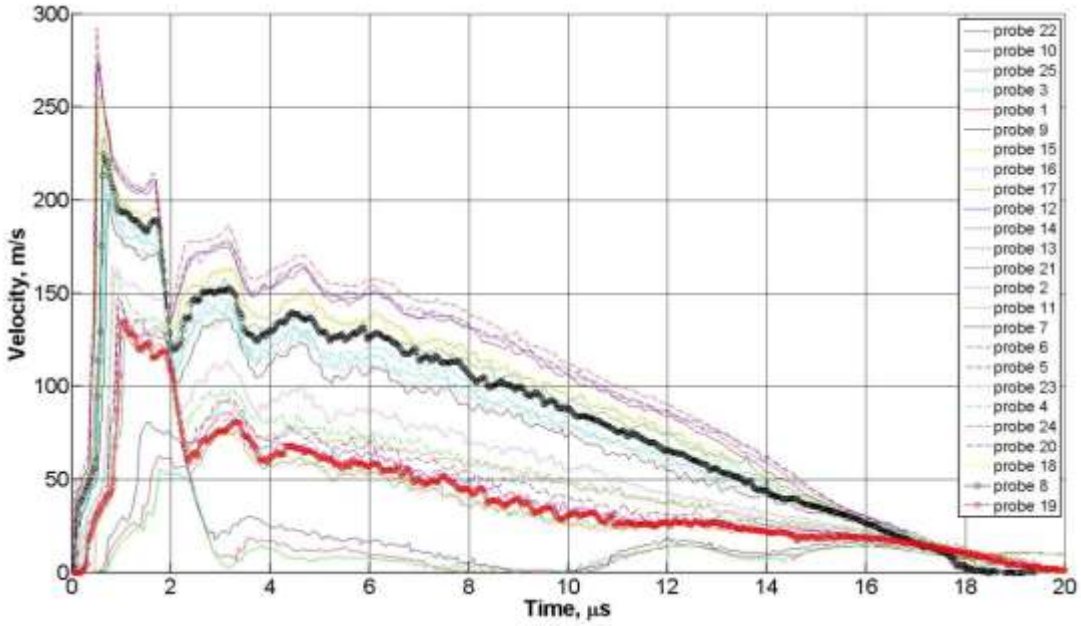

(c) 25-probe MPDV Experiment (Impact Velocity: 5.157 km/s)

Figure 2.35 Typical Free Surface Velocity Profiles of A36 Steel with 25-probe MPDV Arrangements

Table 2.11 Radial Distances of Probes from Impact Center in 11-probe Experiment for 304L (in mm)

	Impact Velocity, m/s
	6583
Impact center distance from plate center	9.96
Probe 1	7.29
Probe 2	4.91
Probe 3	3.03
Probe 4	2.89
Probe 5	4.46
Probe 6	6.99
Probe 7	4.91
Probe 8	3.03
Probe 9	2.88
Probe 10	4.64
Probe 11	6.98

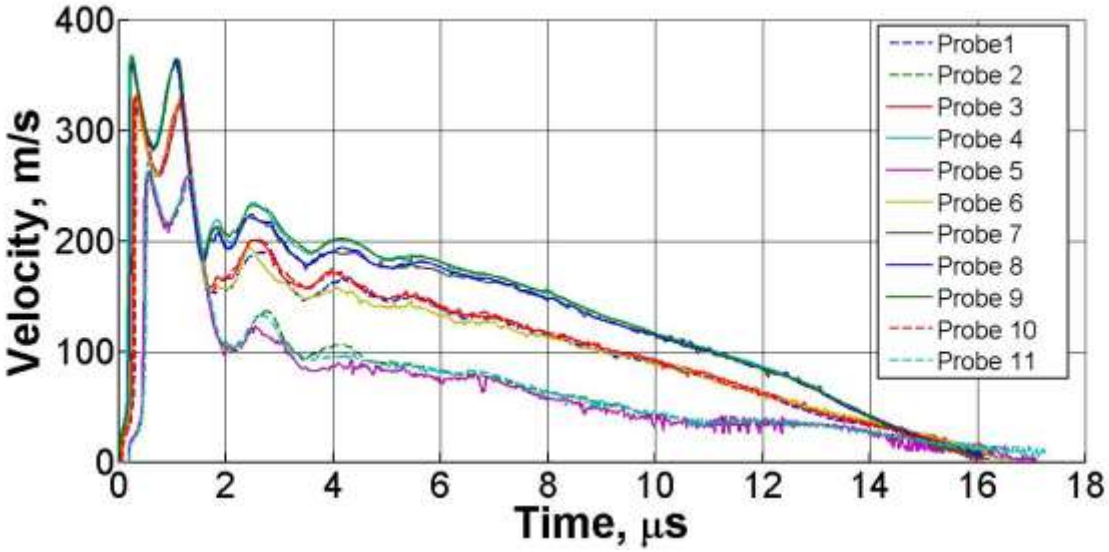

Figure 2.36 Typical Free Surface Velocity Profiles of 304L Steel with 11-probe MPDV Arrangements

Table 2.12 Radial Distances of Probes from Impact Center in 11-probe Experiment for HY100 in mm

	Impact Velocity, m/s
	6689
Impact center distance from plate center	0.02
Probe 1	7.14
Probe 2	4.78
Probe 3	2.96
Probe 4	2.96
Probe 5	4.78
Probe 6	7.14
Probe 7	4.78
Probe 8	2.96
Probe 9	2.96
Probe 10	4.78
Probe 11	7.14

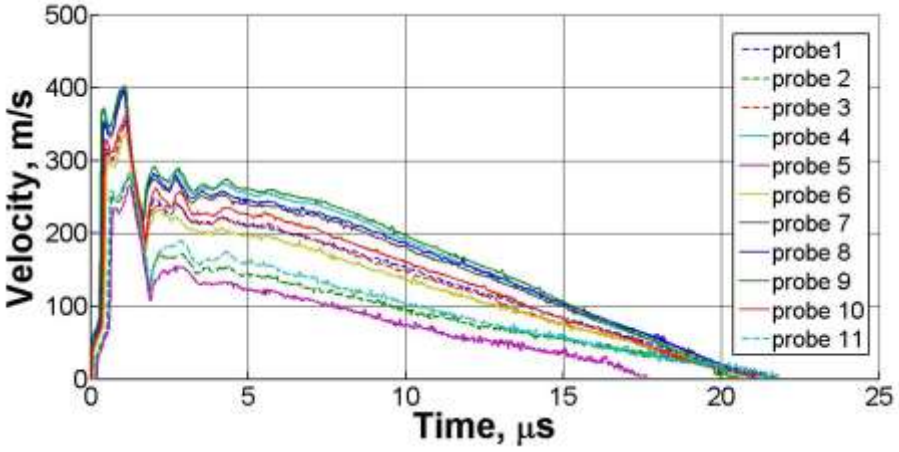

Figure 2.37 Typical Free Surface Velocity Profiles of HY100 Steel with 11-probe MPDV Arrangements

Due to the similar type of velocity profiles for 304L and HY100 steels in 11-probe and 12-probe MPDV experiments, only 11-probe velocity profiles are presented here.

2.7.3 Grouping of MPDV Results

The layout of the MPDV probes, Section 2.6, shows that it can be beneficial to think of the probes in terms of polar coordinates. Therefore, grouping probes with the same radius and average their result will represent the velocity profiles better. Therefore, Table 2.13 and Table 2.14 list the groups for 9-probe and 25-probe MPDV experiment for A36 steel.

Table 2.13 Grouping of Probes in a Typical 9-probe Experiment (Impact Velocity: 4.763 km/s)

Group ID	Probe ID	Average radial distance from impact center, mm	Impact center location in polar coordinates (r, θ°)	Probe# 1 location in polar coordinates (r, θ°)
9-1	1	0.74	(5.47, 35.2)	(5.90, 41.3)
9-2	7, 9	3.92		
9-3	3, 5, 8	5.29		
9-4	2, 4, 6	7.93		

Table 2.14 Grouping of Probes in a Typical 25-probe Experiment (Impact Velocity: 4.823 km/s)

Group ID	Probe ID	Average radial distance from impact center, mm	Impact center location in polar coordinates (r, θ°)	Probe# 1 location in polar coordinates (r, θ°)
25-1	1	0.82	(5.18, 39.5)	(5.59, 47.2)
25-2	2, 3, 4, 5, 6, 7, 8, 9	3.94		
25-3	11, 12, 14, 15, 17, 18, 20, 21	6.57		
25-4	10, 13, 16, 19	9.02		
25-5	22, 23, 24, 25	11.46		

As an example, Figure 2.38 shows the result of averaging velocity profile for probes 2, 4 and 6 in the 9-probe MPDV experiment. This process smoothed some of the ripples that individual probes had exhibited. The results of the grouping process for a typical 9-probe and a typical 25-probe experiments are presented in Figure 2.39 and Figure 2.40 respectively.

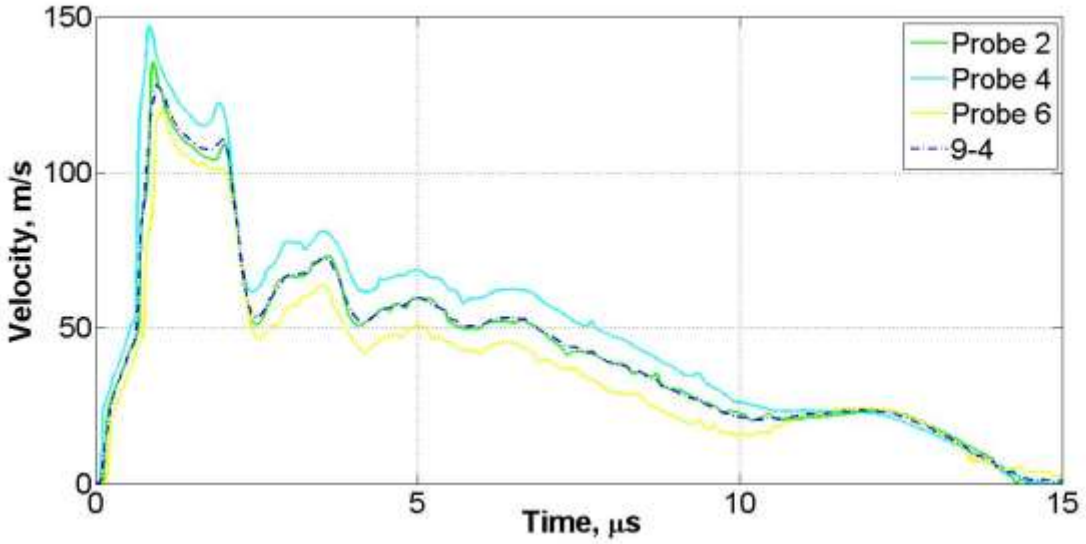

Figure 2.38 Typical Grouping of MPDV Probes in the Case of the 9-probe MPDV Experiment

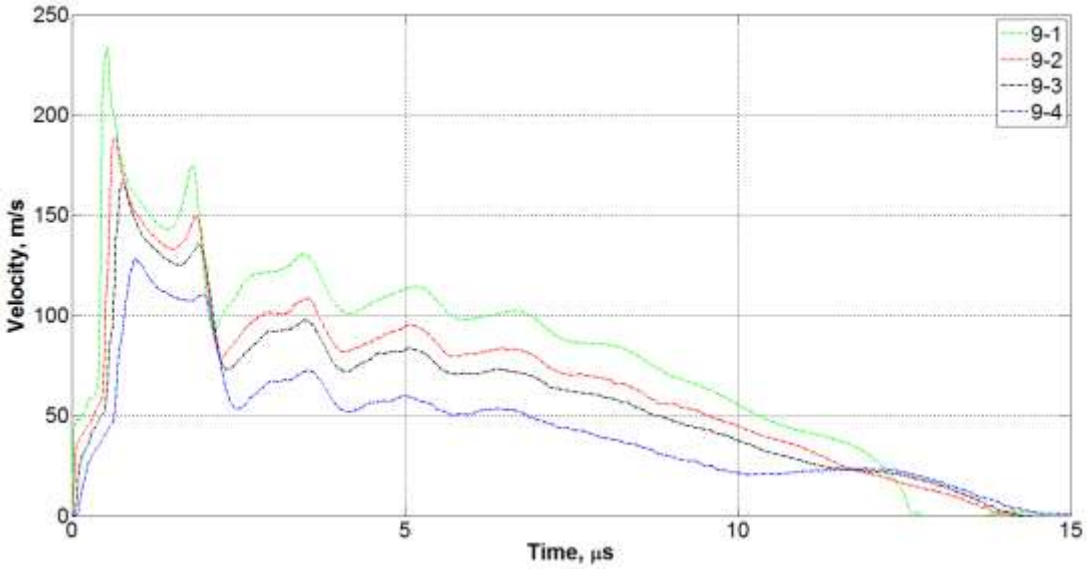

Figure 2.39 Grouping of Free Surface Velocity Profiles of A36 Steel for the 9-probe MPDV Experiment

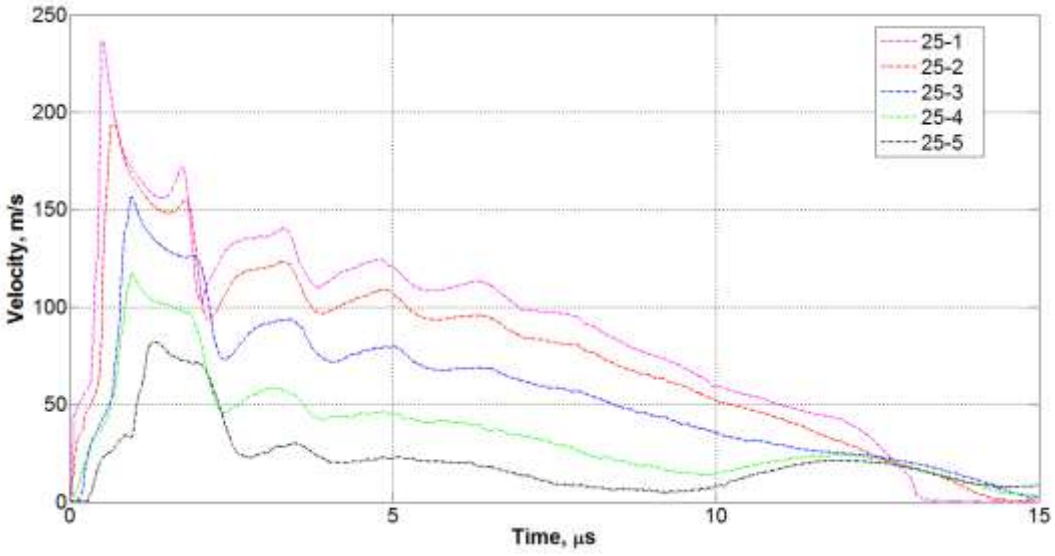

Figure 2.40 Grouping of Free Surface Velocity Profiles of A36 Steel For the 25-probe MPDV Experiment

Similarly, Table 2.15 and 2.16 list the grouping of probes in 11-probe experiment for 304L and HY100 respectively and their corresponding radial distance from plate center and impact center. Note that, plate center (0,0) was considered as datum in all cases. Figure 2.41 and 2.42 represent the average free surface velocities of 304L and HY100 respectively in groups from 11-probe MPDV experiment.

Table 2.15 Grouping of Probes in a Typical 11-probe Experiment for 304L

Group ID	Probe ID	Average radial distance from impact center, mm	Impact center location in polar coordinates (r, θ°)	Probe# 1 location in polar coordinates (r, θ°)
11-1	3,4,8,9	2.96	(9.96, 300.8)	(13.77, 92.1)
11-2	2,5,7,10	4.73		
11-3	1,6,11	7.09		

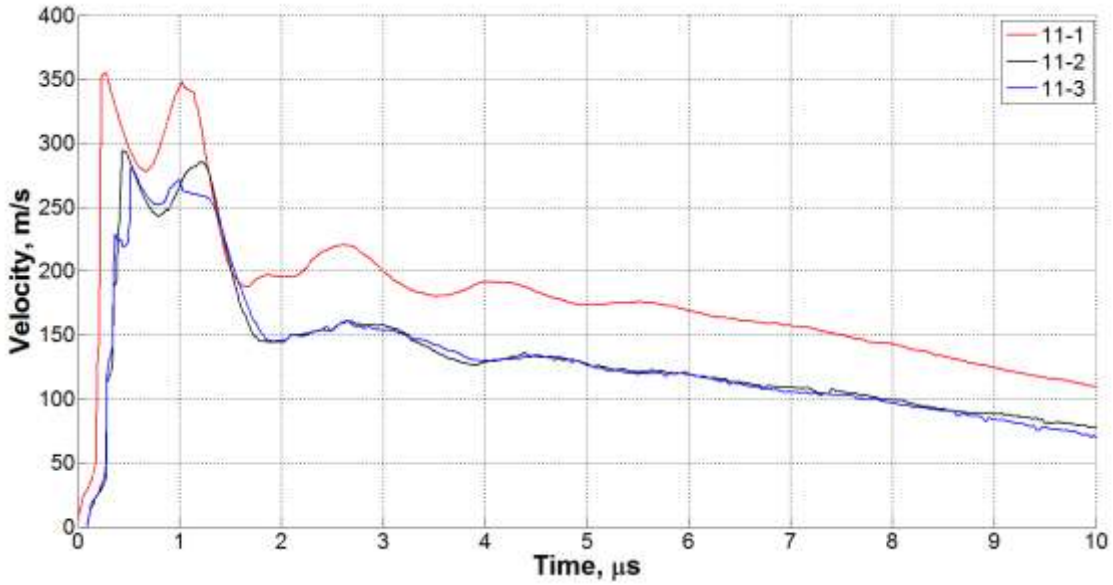

Figure 2.41 Grouping of Free Surface Velocity Profiles of 304L Steel For the 11-probe MPDV Experiment

Table 2.16 Grouping of Probes in a Typical 11-probe Experiment for HY100

Group ID	Probe ID	Average radial distance from impact center, mm	Impact center location in polar coordinates (r, θ°)	Probe# 1 location in polar coordinates (r, θ°)
11-1	3,4,8,9	2.96	(0.02,0)	(7.13, 111.7)
11-2	2,5,7,10	4.78		
11-3	1,6,11	7.14		

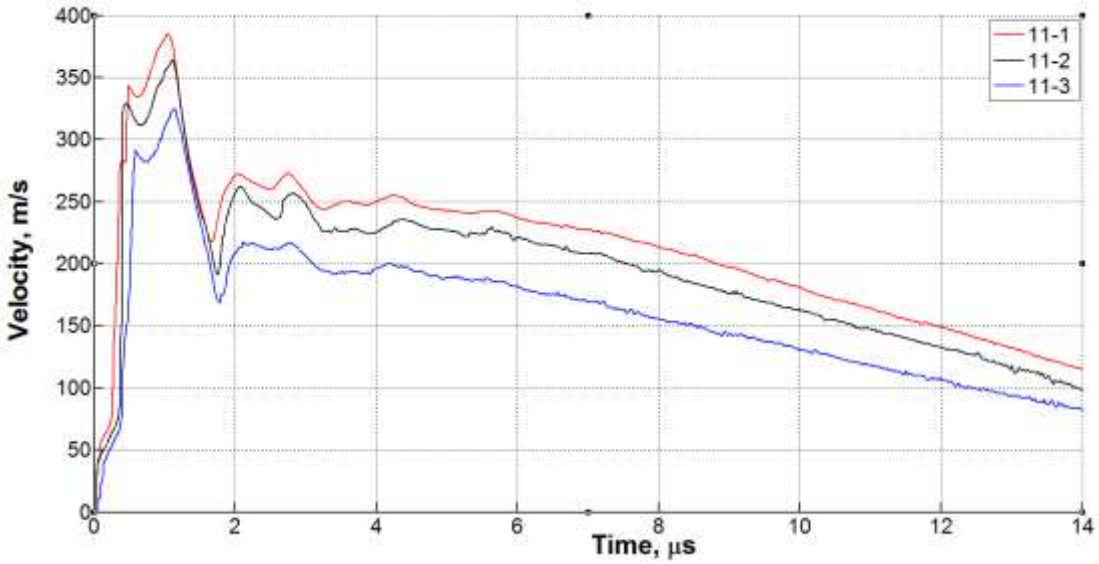

Figure 2.42 Grouping of Free Surface Velocity Profiles of HY100 Steel for the 11-probe MPDV Experiment

CHAPTER 3 FINITE ELEMENT ANALYSIS

3.1 Introduction

Due to the expensive and sophisticated instrumentation of gas gun experiments in hypervelocity conditions, predictive modelling is gaining popularity these days. Therefore, a significant amount of effort has been given to develop different sophisticated computational models and software packages. One of the major objectives of this work is to simulate the gas gun experiments to predict the plastic deformation of the metallic plates. This will help to reduce the experimental need for this kind of material in hypervelocity conditions.

3.2 Hardware and Software

All the computational analysis was done on a 64 GB, 48-core CentOS 4.5 server located at UNLV. The server is capable of parallel processing as this kind of simulation requires long computational time. Commercial dynamic FEA package LS-DYNA v7.0 was used to simulate the experiments. Simulation models were created with LS-DYNA preprocessor v977 []. Models were created using standard unit system for force (N), length (m), mass (kg) and time (s).

3.3 Smoothed Particle Hydrodynamics

Simulating an experiment like projectile impact on a plate at hypervelocity potentially deals with an enormous number of parameters [52]. Under these conditions, extremely high pressure and temperature states are created that make solids behave somewhat like a fluid while

retaining knowledge of their initial strength. In many cases, simulation models include many simplifications for this kind of problem, which can affect the accuracy of such simulations.

SPH was first developed to simulate astrophysical phenomena [53,54]. In SPH method, approximate numerical solution of fluid equations are resolved which can be extended to solve difficult physics problems dealing with material properties. SPH is a meshless numerical technique which can simulate large deformation without much difficulty. Each SPH particle acts as an interpolation point representing density, displacement, acceleration, strain-rate etc. The solution of the entire problem is then computed on all the particles with a regular interpolation function, the so-called 'smoothing length'. The space and time dependent variables determine the 'region of influence' of the neighboring particles.

SPH details have been reviewed time-to-time ever since it was first introduced [55–57]. Very few of them even discussed applying SPH method in hypervelocity impact problems [45,51,58–60]. SPH method already showed superior results compare to ALE and Lagrangian with erosion model in Aluminum plate perforation [61]. Different variables like artificial bulk viscosity, spall strength, particle spacing typically controls the solution of SPH simulation [62,63].

3.4 Model Development

In this work, the experiments were simulated using Lagrangian-based smooth particle hydrodynamics (SPH) solver in LS-DYNA. Initial models of projectiles and target plates were developed by LS Pre-Post 4.1. All the penetration models developed in this work were 2-D axisymmetric model. The reason to choose for an axisymmetric model was that shock response was symmetric as the projectile was impacting in the middle of the plates (roughly) and only first

few instances were experimental interest. Also, SPH algorithm was expensive in terms of computational solution.

Both projectiles and target plates were modeled as SPH. In axisymmetric model, target plate was considered as a cylindrical plate of 76.2 mm radius and 12.7 mm thickness. SPH spacing for both parts in the models was selected in such that mass of each SPH particle in projectile particle was similar to the mass of each SPH particle in the target plate. Extensive particle spacing study was done before developing the model and finally, a particle spacing for 0.05 mm was selected for the target plate to model A36 steel. Details of this particle study is described in APPENDIX F. No boundary conditions were used during the model development. Figure 3.1 represents a typical picture of SPH model developed for each experiment.

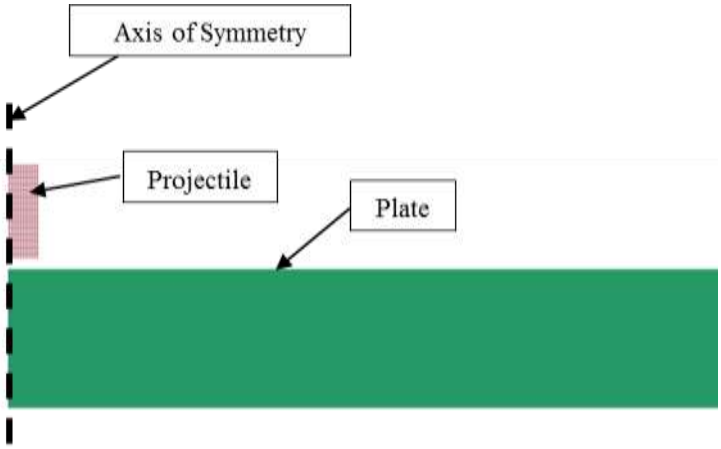

Figure 3.1 Typical Axisymmetric SPH Model

3.5 Material Model

When performing dynamic simulations of this kind, suitable material model must be used that can accommodate high strain rate, large deformations, and temperature effects, which are evident in hypervelocity impact. The Johnson-Cook material model is one of the most effective and commonly used material models for simulating high strain and large deformation problems [64–67]. The Johnson-Cook constitutive equation expresses stress as a function of large strains, high strain-rates and high temperatures [68].

$$\sigma_y = (A + B\bar{\varepsilon}^{p^n})\left(1 + Cln(\dot{\varepsilon}^*)\right)(1 - T^{*m}) \quad (1)$$

where σ_y is the flow stress; A, B, C, n, and m were material constants; ε^p is the effective plastic strain; and $\dot{\varepsilon}^*$ is the effective total strain-rate normalized by quasi-static strain rate. The homologous temperature, T^*, is defined as

$$T^* = \frac{T - T_r}{T_m - T_r}, \quad (2)$$

where, T_r and T_m were room and the melting temperatures in Kelvin, respectively.

In LS-DYNA, a simplified Johnson-Cook model were used without considering any damage parameters. Damage were accommodated with a spall parameter (P_{min}) in Johnson-Cook model. All the parameters of the Johnson-Cook model for Lexan [66], A36 steel [65], 304L [69] and HY100 [70] steel are listed in Table 3.1.

Table 3.1 Johnson-Cook Material Properties for the Projectile and the Target

Material	A (MPa)	B (MPa)	C	M	n	T_m (Kelvin)	$\nu^{\dagger}$
Lexan	75.8	68.9	0	1.85	1.004	533	0.344
A36 Steel	286.1	500.1	0.022	0.917	0.2282	1811	0.260
304L	110	1500	0.014	1	0.36	1694	0.300
HY100	752	402	0.014	1.13	0.36	1793	0.300

† ν is the Poisson's ratio

3.6 Equation of State (EOS)

Materials under shock-wave loading needed a shock model that could account for the sudden pressure, temperature, internal energy, and density changes that occur in front of the shock waves. The equation of state (EOS) of a material is a general thermodynamic relation that is defined by the code user. Various forms of EOS were used to describe the volumetric compression or expansion behavior of different types of materials. One of most commonly used EOS is the Mie-Grüneisen equation of state, which can be expressed [71] as

$$P = \frac{\rho_0 C_0^2 \mu \left(1+\left(1-\frac{\gamma_0}{2}\right)\mu - \frac{a}{2}\mu^2\right)}{\left(1-(S_1-1)\mu - S_2\frac{\mu^2}{\mu+1} - S_3\frac{\mu^3}{(\mu+1)^2}\right)^2} + (\gamma_0 + a\mu)E\,, \tag{3}$$

where, P is the pressure; S_1, S_2, and S_3 are the coefficients of slope of shock velocity-particle velocity curve, γ_0 is the Grüneisen coefficient; a is the volume correction factor; ρ is the instantaneous density, C_0 is the Hugoniot intercept of the metal; E is the internal energy; and μ =

($\rho/\rho_0 - 1$) where ρ_0 is the reference density. For materials under compression, a temperature-corrected form of the above equation is given below [72].

$$P = \frac{\rho_0 C_0^2 \mu \left(1+\left(1-\frac{\gamma_0}{2}\right)\mu\right)}{(1-(S_1-1)\mu)^2} + \gamma_0 E \quad (4)$$

Assuming a negligible change in density and internal energy, the above equations can be rewritten as

$$P = \frac{\rho_0 C_0^2 \left(2-\frac{\gamma_0}{2}\right)}{(1-S_1)^2}. \quad (5)$$

Both LS-DYNA and CTH included a Grüneisen EOS for Lexan, A36 steel, 304L and HY100; these were used in simulations during this study, using the input parameters listed in Table 3.2.

Table 3.2 EOS Parameters for the Projectile and the Target

Material	ρ_0 (kg/m^3)	C_0 (m/s)	S_1	γ_0
Lexan [73]	1190	1933	1.42††	0.61
A36 Steel [67]	7890	4569	1.49	2.17
304L [74]	7900	4570	1.49	1.93
HY100 [75]	7746	3574	1.92	1.69

†† S_1 value for Lexan is suggested as 1.42 [55]

3.7 Estimation of the Hugoniot Elastic Limit and Spall Strength

In most fundamental shock studies, velocimetry data are obtained from uniaxial strain experiments on the shock Hugoniot. This work considered the case of a projectile-plate penetration experiment that can be described using axisymmetric assumptions. The Hugoniot elastic limit and spall strength were calculated based on the uniaxial case in the absence of axisymmetric data. Spall strength is defined by a P_{min} value in Johnson-Cook material model in LS-DYNA.

The approximate Hugoniot elastic limit, σ_{HEL}, and spall strength, σ_{spall}, of A36 steel were calculated from this velocity profile by assuming that the impact was a one-dimensional localized phenomenon with the following relations [26]:

$$\sigma_{HEL} = \frac{1}{2}\,\Delta U_H \rho_0 c_l\ , \tag{6}$$

$$\sigma_{spall} = \frac{1}{2}\,\Delta U_{fs} \rho_0 c_b\ , \tag{7}$$

where ΔU_H was the free-surface velocity at elastic precursor wave; ΔU_{fs} was the pullback velocity of free surface as shown in Figure 3.2; and c_l and c_b correspond to the longitudinal and bulk sound speed, respectively.

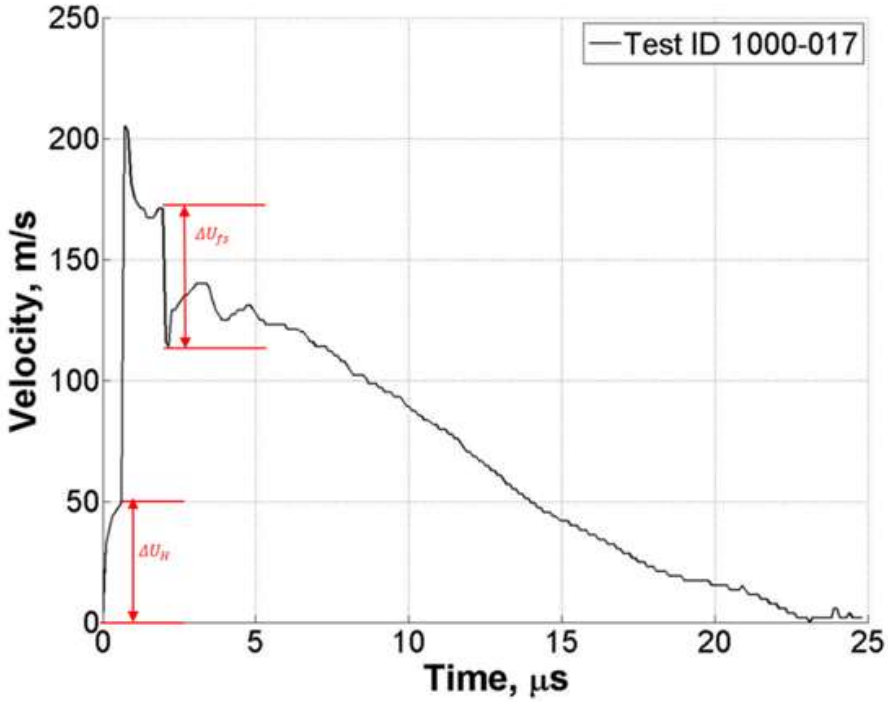

Figure 3.2 Spall Strength Calculation from Free Surface Velocity Profiles

These speeds depend on the Young's modulus, *E*, and the bulk modulus, *K*, of all the steels experimented. Equations are given below.

$$c_l = \sqrt{\frac{E}{\rho}} \tag{8}$$

$$c_b = \sqrt{\frac{K}{\rho}} \tag{9}$$

Based on these equations, the Hugoniot elastic limit and the spall strength of A36 steel are approximated based the experiments and the above analysis; results are shown in Table 3.3.

Table 3.3 Spall Strength Calculation of A36 Steel from a Typical 9-probe MPDV Experiment

	Probe 1	Probe 2	Probe 3	Probe 4	Probe 5	Probe 6	Probe 7	Probe 8	Probe 9
ΔU_H (m/s)	15.62	25.74	27.14	29.61	29.77	47.16	22.04	21.72	23.12
σ_{HEL} (GPa)	0.31	0.51	0.54	0.59	0.59	0.94	0.48	0.43	0.46
ΔU_{fs} (m/s)	81.72	57.55	63.72	60.54	61.29	54.76	70.31	63.49	70.13
σ_{spall} (GPa)	1.36	0.96	1.06	1.01	1.02	0.91	1.17	1.06	1.17

Similarly, Table 3.4 lists all the spall strength values of A36 steel calculated for typical 25-probe MPDV experiment.

Table 3.4 Spall Strength Calculation of A36 Steel from a Typical 25-probe MPDV Experiment

	Probe 1	Probe 2	Probe 3	Probe 4	Probe 5	Probe 6	Probe 7	Probe 8	Probe 9	Probe 10	Probe 11	Probe 12	Probe 13
ΔU_H (m/s)	17.52	27.39	28.18	28.68	23.22	18.76	9.70	12.48	22.46	16.10	27.57	28.57	19.52
σ_{HEL} (GPa)	0.35	0.54	0.56	0.57	0.46	0.37	0.19	0.25	0.45	0.33	0.55	0.57	0.39
ΔU_{fs} (m/s)	68.9	63.56	63.53	60.82	62.02	61.78	59.86	64.08	67.82	59.41	56.3	53.81	51.93
σ_{spall} (GPa)	1.14	1.06	1.06	1.01	1.03	1.03	0.99	1.06	1.13	0.99	0.94	0.89	0.86
	Probe 14	Probe 15	Probe 16	Probe 17	Probe 18	Probe 19	Probe 20	Probe 21	Probe 22	Probe 23	Probe 24	Probe 25	
ΔU_H (m/s)	36.86	22.07	19.72	29.15	26.66	31.21	38.5	22.73	20.53	14.45	14.67	9.82	
σ_{HEL} (GPa)	0.73	0.44	0.39	0.58	0.53	0.62	0.77	0.45	0.41	0.29	0.29	0.20	
ΔU_{fs} (m/s)	53.13	52.57	49.01	59.04	52.46	52.62	57.96	54.92	53.62	47.03	46.04	49.54	
σ_{spall} (GPa)	0.88	0.87	0.81	0.98	0.87	0.87	0.96	0.91	0.89	0.78	0.77	0.82	

Hence, in all simulations of A36 steel experiments, an average value of 9-probe and 25-probe MPDV experiments were chosen which was 0.98 GPa.

Similarly, spall strength was calculated for 304L and HY100 from 11-probe experiments and an average value was used simulating these experiments for each of these steel individually. Table 3.5 and Table 3.6 lists spall strength of 304L and HY100 from typical 11-probe MPDV experiments.

Table 3.5 Spall Strength Calculation of 304L Steel from a Typical 11-probe MPDV Experiment

	Probe 1	Probe 2	Probe 3	Probe 4	Probe 5	Probe 6	Probe 7	Probe 8	Probe 9	Probe 10	Probe 11
ΔU_{fs} (m/s)	167.7	150.8	163.1	168.9	151.3	161.7	163.7	175.7	169.5	166.8	150.1
σ_{spall} (GPa)	3.05	2.74	2.96	3.07	2.75	2.94	2.97	3.19	3.08	3.03	2.73

Table 3.6 Spall Strength Calculation of HY100 Steel from a Typical 11-probe MPDV Experiment

	Probe 1	Probe 2	Probe 3	Probe 4	Probe 5	Probe 6	Probe 7	Probe 8	Probe 9	Probe 10	Probe 11
ΔU_{fs} (m/s)	164.0	134.5	158.7	169.7	143.4	140.6	163.4	167.1	175.4	162.0	140.2
σ_{spall} (GPa)	2.99	2.46	2.90	3.10	2.62	2.57	2.98	3.05	3.20	2.96	2.56

The average spall strength values of 304L and HY100 were 2.95 GPa and 2.85 GPa taken respectively for simulations. Spall strength of these three steels can be correlated with their ultimate tensile strength (listed in Table 2.2). Higher ultimate tensile strength steel showed higher spall strength.

3.8 Simulation Results

In all LS-DYNA simulations, projectiles disintegrated upon impact with the target parts. Target plates showed a crater and a small bulge on the back surface of the plates like the experiments. Spall crack planes were also developed during the simulations. Figure 3.3 and Figure 3.4 represents the crater and bulge formation and spall crack formation respectively.

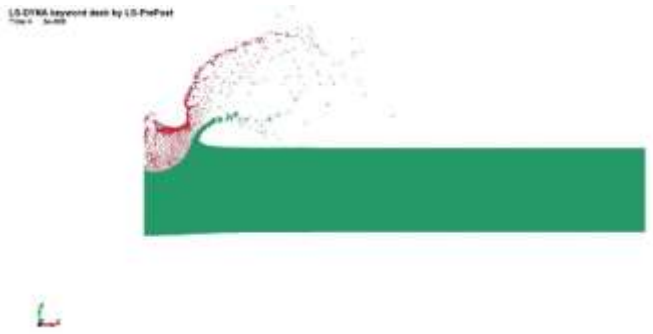

Figure 3.3 Crater and Bulge Formation in Typical Simulation of A36 Steel in 9-Probe MPDV Experiment (Impact Velocity: 4.763 km/s)

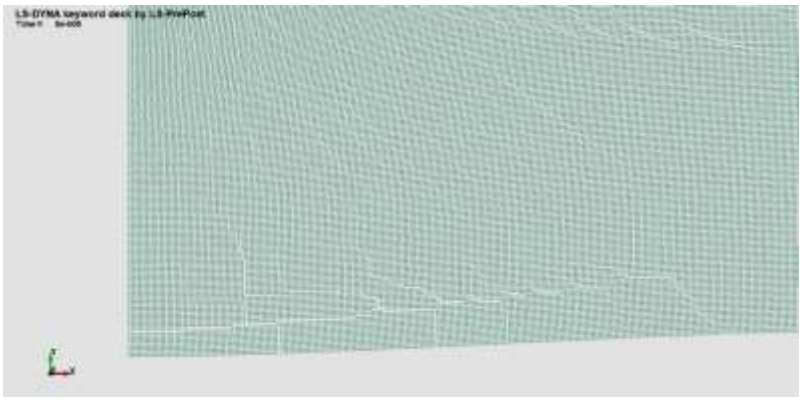

Figure 3.4 Spall Plane Formation in Typical Simulation (Zoomed In View of Figure 3.3)

After each simulation, crater diameter and depth, height of bulge were measured. These measurements were than compared to the corresponding experimental measurements. Note that, this spall plane location and width were depended on the simulation runtime: longer the runtime, longer the width and height of the spall cracks. Table 3.7 lists the details of the crater and bulge from SPH simulation for selected experiments.

Table 3.7 Typical LS-DYNA Simulation Results for Selected Experiments

Materials	MPDV Arrangements	Impact velocity, km/s	Crater diameter, mm	Crater depth, mm	Bulge, mm
A36	9-probe	4.763	16.2	4.8	1.4
	25-probe	4.823	16.3	4.8	1.5
304L	11-probe	6.583	16.7	5.9	1.8
HY100	11-probe	6.698	16.8	5.7	2.0

Free surface velocity profiles were collected based on the radial distance of the probe groups. Typical free surface velocity profile from few MPDV experiments are presented in Figure 3.5 to Figure 3.8.

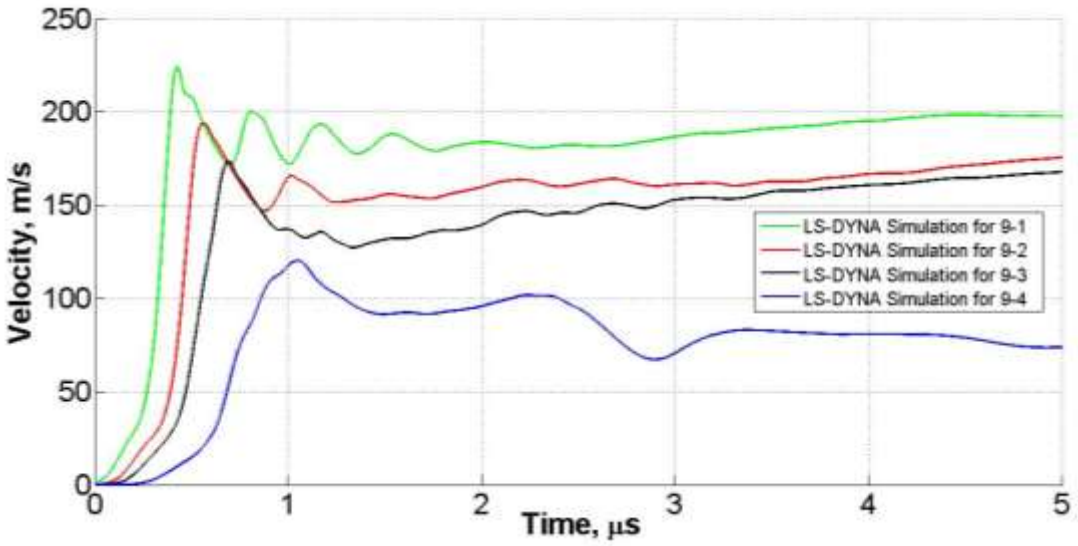

Figure 3.5 Simulated Velocity Profiles of A36 Steel for 9-probe MPDV Experiment (Impact Velocity: 4.763 km/s)

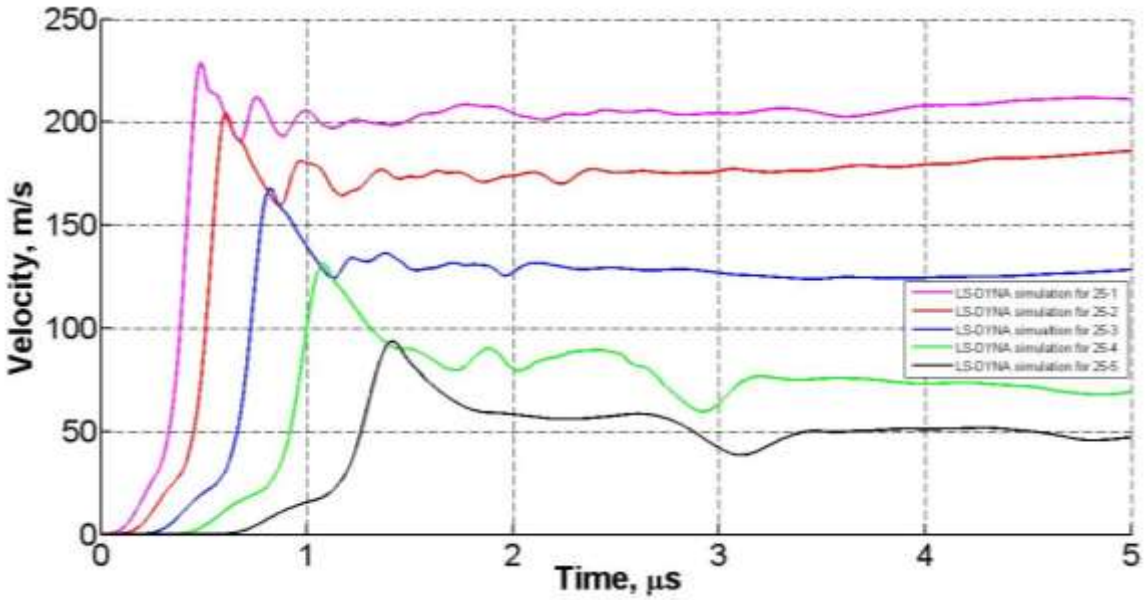

Figure 3.6 Simulated Velocity Profiles of A36 Steel for 25-probe MPDV Experiment (Impact Velocity: 4.823 km/s)

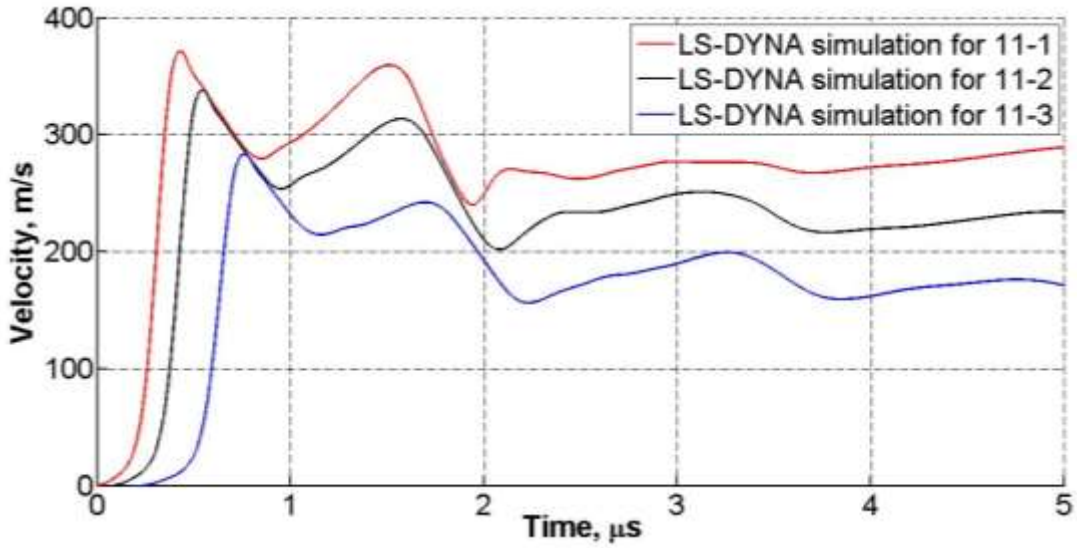

Figure 3.7 Simulated Velocity Profiles of 304L Steel for 11-probe MPDV Experiment (Impact Velocity: 6.583 km/s)

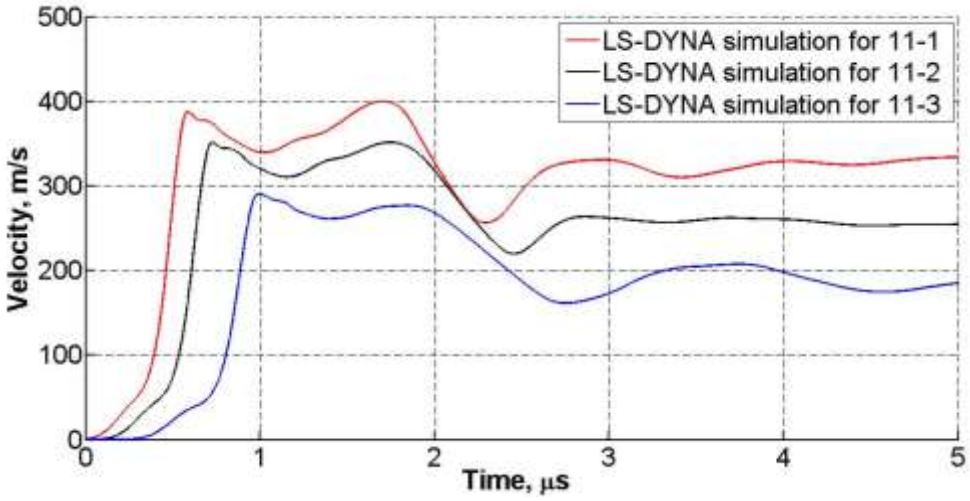

Figure 3.8 Simulated Velocity Profiles of HY100 Steel for 11-probe MPDV Experiment (Impact Velocity: 6.689 km/s)

All of these velocity profiles are presented up to 5 μs as most of the characteristic features are captured by that time. Velocity profiles showed a two peak wave-structure and HEL with a sharp plastic rise. Also, pullback velocity presented in the wave represented the spall crack formation in simulations.

CHAPTER 4 RESULTS COMPARISON & DISCUSSION

4.1 MPDV Probe Arrangements

In this work, different types of MPDV probe arrangements were used. One of the primary purposes of this work was to explore the capability of MPDV systems and compare different MPDV probe arrangements. As far as the results presented earlier clarifies the fact that MPDV system was able to capture free surface velocities from multiple points at the same time. Therefore, in order to check the MPDV performance, MPDV probe arrangements were evaluated for same material. In this case, one of the 9-probe experiment and 25-probe experiment for A36 were compared. Results of the peak velocities from these experiments were plotted against radial distance of the probe to check the consistency of the collected velocimetry data (Figure 4.1).

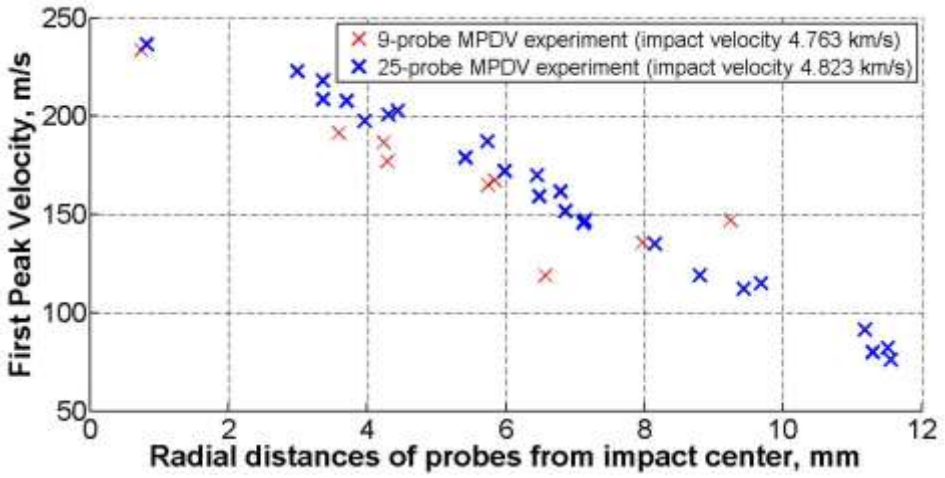

Figure 4.1 Free Surface Velocity vs. Radial Distances of Probes from Impact Center in 9-probe and 25-probe MPDV Experiments for A36 Steel

From the above figure, it is clear that peak velocities decreases as the radial distances from the impact center increases. There are few certain deviations though; which may be due to the development of spall crack inside. Higher number of probes ensures the capture of the velocimetry data uniformly.

4.2 LS-DYNA Simulation Results Comparison

All LS-DYNA simulations results were compared to experimental results to verify the accuracy of the FEA models developed. Simulation results were compared in terms of physical measurements, free surface velocities with the corresponding MPDV experiments.

4.2.1 Physical Measurement Comparison

Similar to experiments, all LS-DYNA simulations showed crater, bulge and spall crack formation. Simulation results were depended on the run time, especially for the crater depth, bulge and spall crack formation. Longer run time typically ensures a much closer match to the experimental results. But, as mentioned earlier, due to the higher computational time and expense, most of the simulations were run only for first few microseconds to capture the free surface velocity profile details. Table 4.1 lists a comparison of all the physical properties. Simulation results of A36 steel were very well matched with both 9- and 25- probe MPDV experiments in terms of crater and bulge details; difference ranging from 0%-26%. In case of 304L and HY100 steel, difference for crater diameter and depth were -2.4%-11% whereas difference ranged from 4.2%- 33% for bulge.

Table 4.1 Typical Comparison of Simulation Results with Selected Experiments (after 20 μs simulation)

Material	MPDV Experiment	Impact Velocity, m/s	Crater Diameter, mm			Penetration Depth, mm			Bulge, mm		
			Exp.	FEA	% Difference	Exp.	FEA	% Difference	Exp.	FEA	% Difference
A36	9-probe	4763	15.4	16.2	-5.2	6.5	5.7	12.3	1.4	1.4	0
	25-probe	4823	15.1	16.3	-7.9	6.5	5.8	10.8	1.5	1.5	0
304L	11-probe	6583	17.3	16.7	3.5	6.4	5.9	7.8	2.4	2.3	4.2
HY100	11-probe	6698	16.5	16.9	-2.4	6.4	5.7	10.9	3.0	2.7	10

4.2.2 Free surface velocity comparison

Free surface velocity profiles from the above simulations were compared with selected MPDV experiments. To compare the free surface velocity profiles between simulation and experimental results, the discussion was narrowed down to the velocity during the first 5μs after impact where most important features occurred: (a) elastic precursor and Hugoniot elastic limit (HEL), (b) plastic wave (c) peak velocity (d) spall signatures.

Figure 4.2 shows a typical comparison of simulated velocity profiles with experimental velocity profile for a typical 9-probe MPDV experiment with an impact velocity of 4.763 km/s. In order to better understand the comparison, only the velocity profile close to the impact center was compared and presented below.

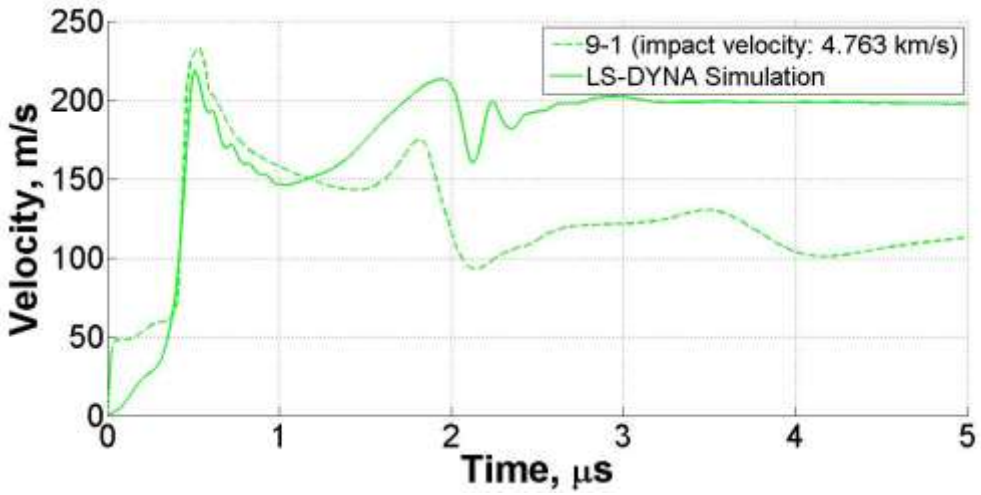

Figure 4.2 Free Surface Velocity Profile Comparison of Center Probe in a Typical 9-probe MPDV Experiment for A36 Steel

The result showed that LS-DYNA simulation were able to capture the elastic precursor in a two-peak velocity profiles as observed in the experiment. But, the simulation showed lower HEL. For the 4.763 km/s MPDV test, the HEL calculated from free surface velocity profile was approximately 1.25±0.2 GPa. Free surface velocities from LS-DYNA showed HEL of A36 steel as 0.64 GPa for this experiment. Simulation also captured the sharp rise in plastic wave almost identical to the experimental velocity profile. LS- DYNA simulations registered almost same magnitude for the first peak in the experiment (6% lower velocity) but showed much higher velocity for second peak.

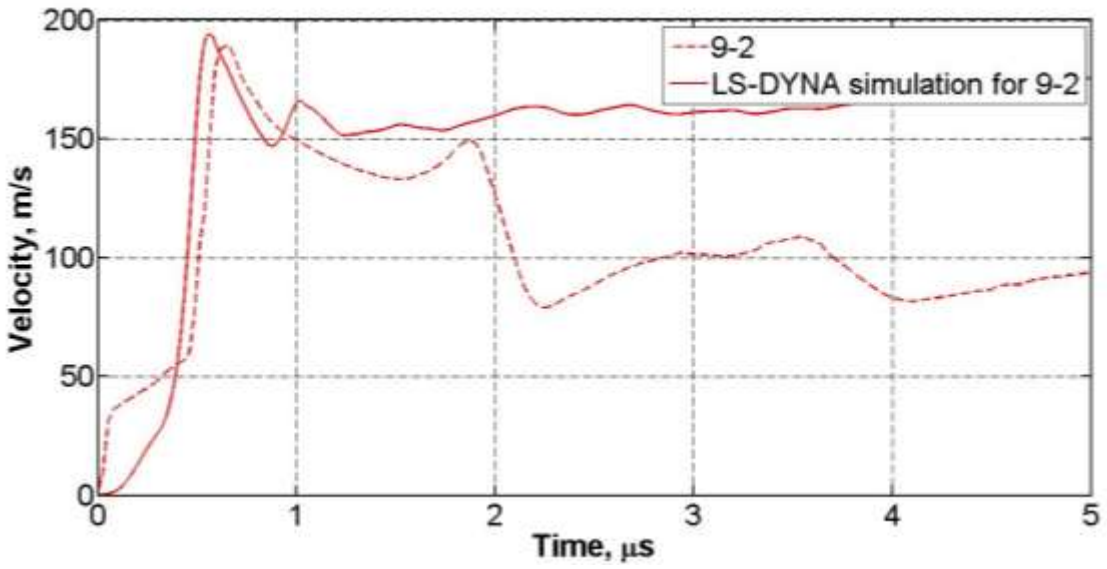

(a)

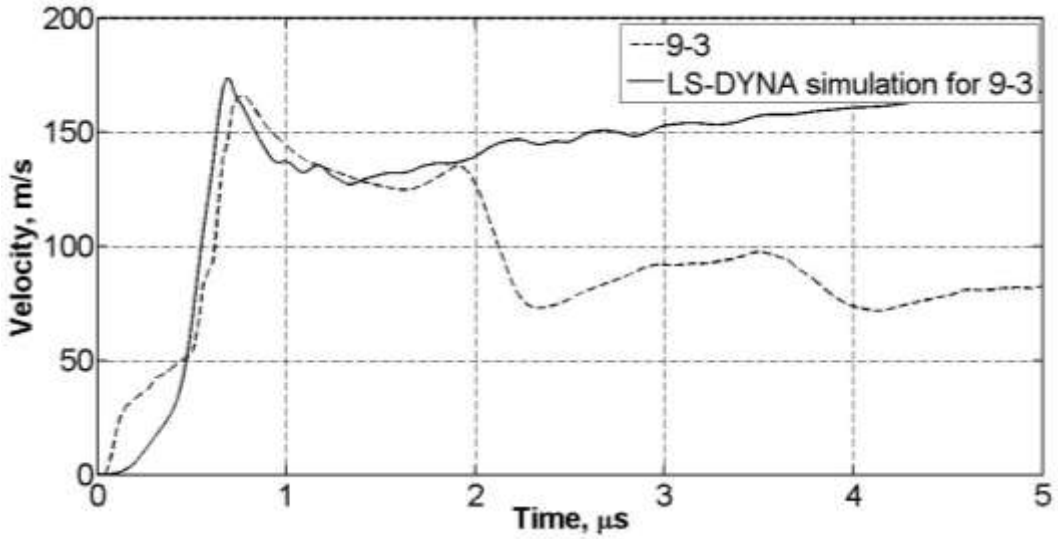

(b)

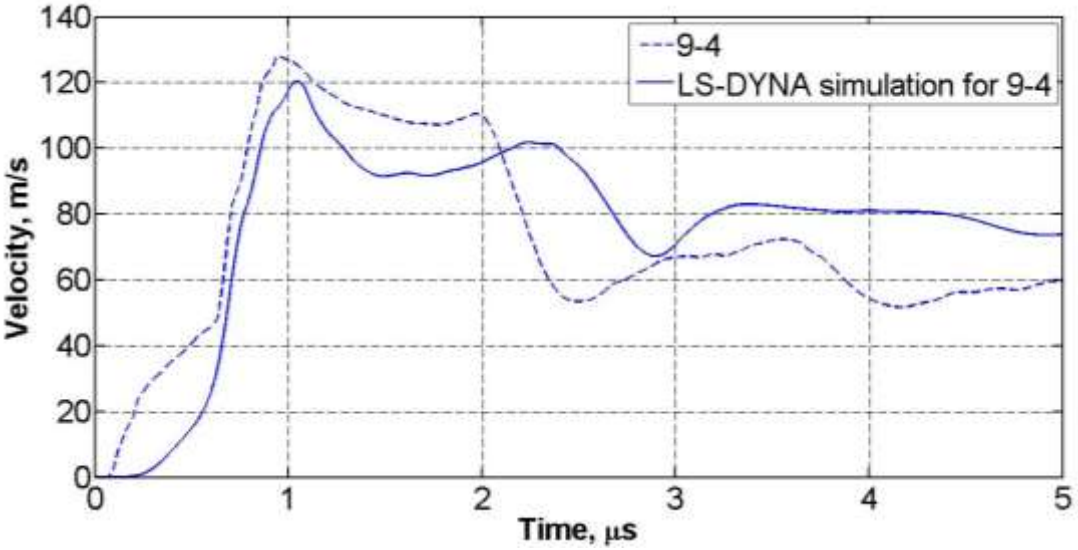

(c)

Figure 4.3 Free Surface Velocity Profile Comparison of Grouped Probes in a Typical 9-probe MPDV Experiment for A36 Steel (Impact Velocity: 4.763 km/s)

Free surface velocity profiles from the rest of the grouped probes were compared with LS-DYNA simulation in Figure 4.3 for the 9-probe MPDV experiment. All of these simulated velocity profiles captured the elastic precursor wave, HEL, plastic wave. Spall signatures were not prominent in Figure 4.3 (a) and (b). The reason behind this anomality was due to the fact that once spall happened in SPH model in LS-DYNA, all the elements associated with the spall plane and behind it felt no pressure. This is a typical feature in SPH modeling in LS-DYNA. Hence, elements considered for the same radial distances of those grouped probes did not feel any pressure wave once the spall happened earlier and did not register any spall signature. In case of Figure 4.3 (c), element considered for free surface velocity was not affected by the spall crack plane propagation. Hence, there was clear spall signatures registered in simulated velocity profile in Figure 4.3 (c).

In case of 25-probe MPDV experiments for A36 steel, LS-DYNA simulations were able to capture all the major features of the free surface velocity profiles as discussed above. Magnitude of the peak velocities, HEL, spall strengths were different from the experiment though; as most of the simulations were run for a shorter time due to the long computational time.

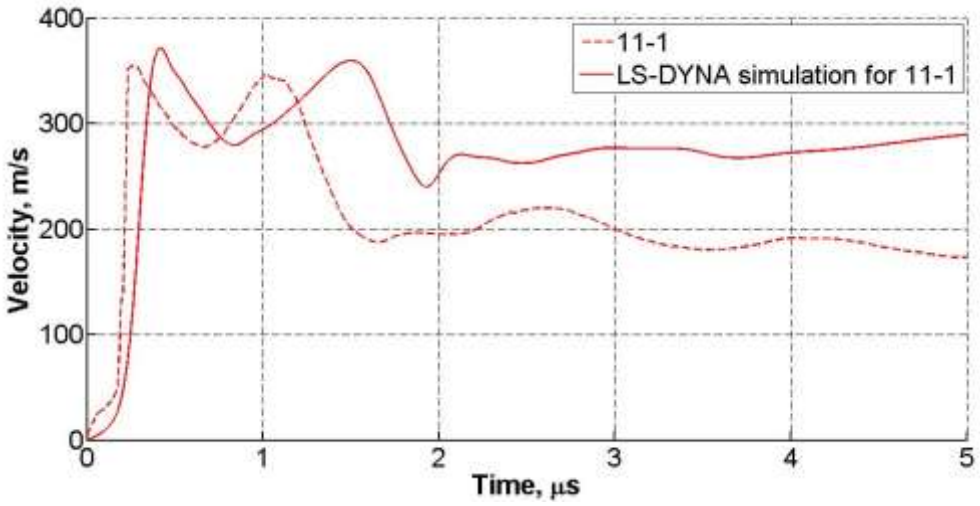

(a)

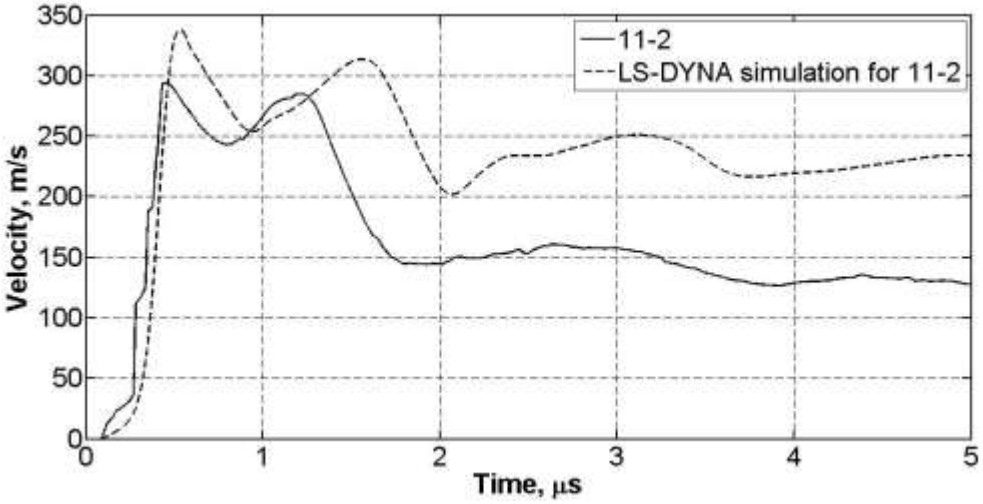

(b)

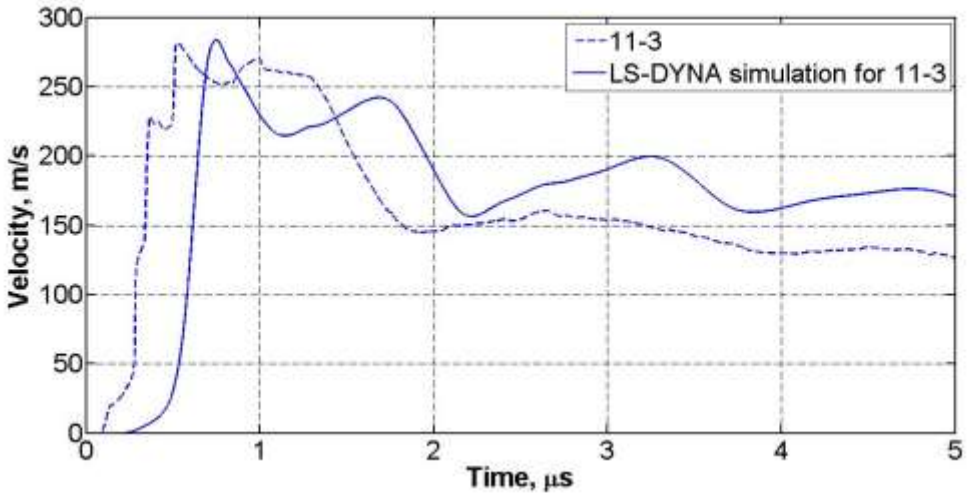

(c)

Figure 4.4 Free Surface Velocity Profile Comparison of Grouped Probes in a Typical 11-probe MPDV Experiment for 304L Steel (Impact Velocity: 6.583 km/s)

Figure 4.4 presents free surface velocity profile comparison of a typical 11-probe MPDV experiment for 304L steel. Similar to 11-probe experiment, all the simulated velocity profiles captured elastic precursor wave, HEL, sharp rise in plastic wave, peak velocities and spall strength signatures. Although, simulated velocity profiles were much delayed in the rise. All simulated velocity profiles registered lower HEL from experiment which differed from 13.4%-26.6%. All profiles captured higher peak velocities for the 1st peak and the difference was between -4.8% to -15.2%.

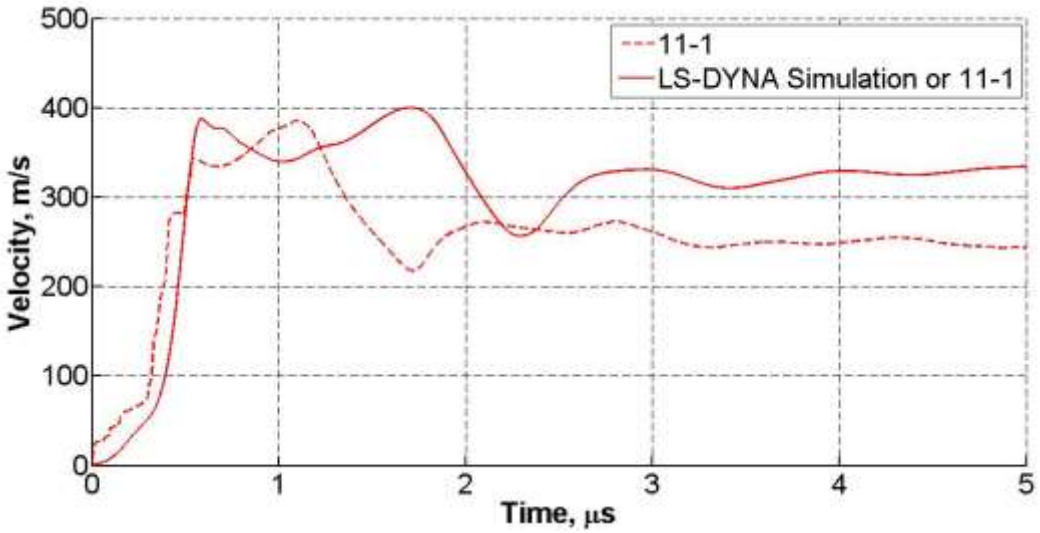

(a)

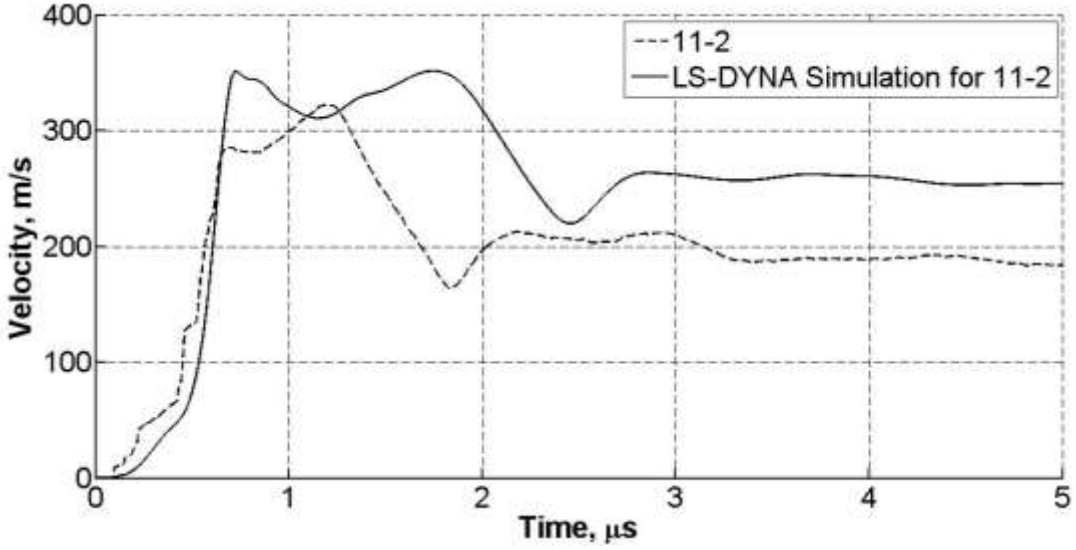

(b)

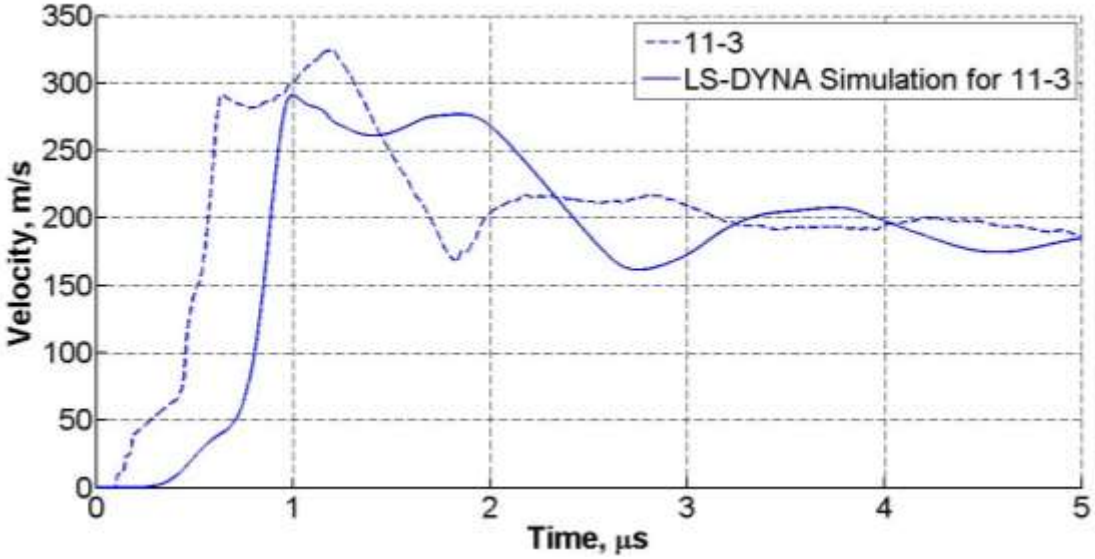

(c)

Figure 4.5 Free Surface Velocity Profile Comparison of Grouped Probes in a Typical 11-probe MPDV Experiment for HY100 Steel

Figure 4.5 presents free surface velocity profile comparison of a typical 11-probe MPDV experiment for HY100 steel. Similar to A36 and 304L simulations, all these simulated velocity profiles captured elastic precursor wave, HEL, sharp rise in plastic wave, peak velocities and spall strength signatures like the 11-probe MPDV experiments of HY100 steel.

Although, all of these simulations captured the basic characteristics of free surface velocity profiles; there were few differences as discussed above. A good explanation for this mismatch was that parameters of Johnson-Cook material model and Mie-Gruneien EOS model used in simulations were mostly developed in uniaxial conditions. Although; the fundamental shock physics nature of a material in dynamic conditions can be explained by these model parameters; these parameters were unable to explain all the distintive phenomena of material in nonuniaaxial conditions.

Simulation results could also vary due to the fact that all the other parameters chosen for SPH model in LS-DYNA may have some limitations. In simulations of HY100 steel, velocity profiles were supposed to capture a second peak in the plastic wave. But, due to the lack of capability of phase transition model in SPH solver in LS-DYNA; a second EOS for ε-iron was not added.

4.3 Comparison of Free Surface Velocity Profiles of A36, 304L and HY100

This study was initially started to explore the deformation behavior of A36 steel in hypervelocity conditions. Experiments were designed with gas gun incorporating MPDV diagnostic system. Initial velocimetry data of A36 steel from MPDV system, raised one of the primary question: Does A36 steel goes to reversible α↔ε phase transition like all other low carbon

steels [76]? The reason behind this concern was that whether or, not phase transition model needed to be incorporated in simulation models. A good way to answer this question was to perform a detail microscopic work on the post-test target samples. That was beyond the scope of this project and was picked by another fellow researcher in the team to explore the microscopic behavior [77]. Another alternative way was to explore two known well characterized materials- one with this type of pressure induced phase transition and another without phase transition and test them under the same hypervelocity conditions to collect their velocimetry data. Then, free surface velocity profiles of this two materials were to compare with the free surface velocity profile of A36 steel. This approach was thought to clarify the primary concern.

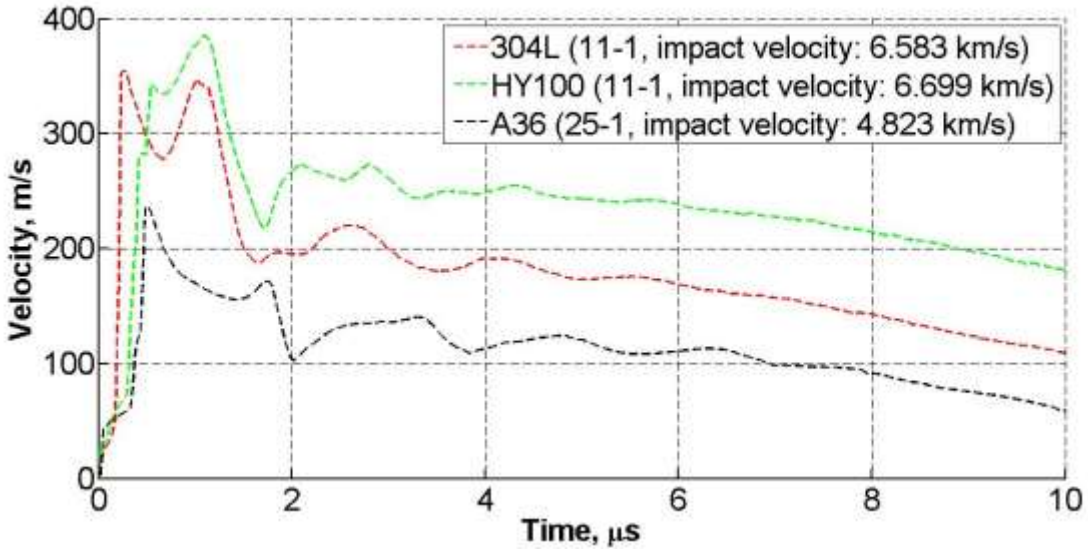

Figure 4.6 Typical Comparison of Free Surface Velocity Profiles for 3 Materials

To understand the velocity profiles of A36 better, all of these three materials velocity profiles were compared in Figure 4.6. This figure showed only the velocity profiles of first group of MPDV probes as they were closest to the impact center. In the figure, 304L and HY100 showed

high magnitude of first peak velocity than A36. This was due to higher impact velocity of those experiments. Apart from this, all of these velocity profiles showed two-wave peaks with elastic precursor, HEL and spall signature. 304L and A36 steel showed almost similar fashion first peak velocity rise; although plastic wave rise was slower in A36 steel. Then there was a sharp drop in the velocity profiles for both 304L and A36 steel; followed by a second rise in the peak. On the other hand, HY100 profiles showed a lower first peak velocity and a higher magnitude second peak velocity. The exact reason for these behavior was not properly understood during this study and certainly demands further exploratory research work. This could be due to asymmetric nature of the stress wave and certain feature contributed from pressure-induced phase transition. But, a strong signature of pressure-induced phase transition signature was not present in HY100 steel and so was in A36 profiles. Although, this comparison didn't clarify the concern confidently; but were able to highlight the distinctions in free surface velocity profiles between HY100 and 304L. Further study done by this research group proved the pressure-induced phase transition in A36 steel [77].

CHAPTER 5 CONCLUSION & FUTURE WORK

This chapter highlights the overall summary of the research performed to achieve the project objectives. Also, provides few recommendations for the future work that would lead to explore new challenges in this area.

As discussed, hypervelocity impact events possess great challenges in terms of experimental set up in laboratory settings and requires sophisticated instrumentation. This type of experiments provide extensive data on the dynamic behavior of materials which can be used to design structures in extreme conditions like ballistic events and meteorite impact and so on. Most of the well-known materials behave significantly different in hypervelocity conditions. This study focused to explore the plastic deformation behavior of commonly used structural material A36 steel in hypervelocity conditions and later extended the idea to study two other different steel behaviors: 304L and HY100.

To explore the plastic deformation behavior, a simple plate penetration problem was designed with a two-stage light gas gun where a projectile hit the target plate with a velocity range of 4.5-6.7 km/s. Experiments were designed in such way that instead of making a complete penetration of the target plate upon impact, a plastically deformed bulge arise on the back side of the target plate. After all experiments, target plates were monitored for crater and bulge details.

Acquiring data from this type of impact events is always a challenge. Several sophisticated instruments have been developed so far in past few decades. MPDV is one of the new addition to this diagnostic innovation race. Exploring the capability of MPDV system in this type of experiment was one of the primary goals of this study. Hence, all gas gun experiments in this study

were performed with the incorporation of MPDV system to collect the velocimetry data. Different type of MPDV probe arrangements were trialed. MPDV system were operated by the NSTec field crew in all experiments. Data were extracted in the NSTec facility with the tools developed by NSTec team. This extracted data were then handed over to UNLV team for further analysis. MPDV data analysis revealed detail features of the materials which helped to understand the deformation behavior of these steels in dynamic conditions.

One of the key objectives of this study was to simulate this hypervelocity impact experiments with existing FEA tools. 2-D axisymmetric model of projectile and target plates were developed in LS-DYNA SPH solver. SPH technique provided unique advantage over the traditional mesh based Lagrangian method as particles were able to behave like fluid in such high impact velocity of projectile. Models were incorporated with a Johnson-Cook material model to accommodate the large strain rates, and deformations in such experiments. To capture the shock properties of the material, Mie-Gruneisen EOS was used in this model. Spall strength value was calculated with a one-dimensional impact assumption from the experimental results for each material and was used in the corresponding simulations.

Simulation results were compared with the physical details of crater and bulge and also with free surface velocity profiles. Crater and bulge information were in reasonable agreement with all simulation results. All the simulated free surface velocity profiles captured the basic features like elastic precursor, HEL, plastic wave rise, peak velocities, spall strength signature and so on. In Chapter 4, all of these features were compared with the experimental velocity profiles. Note that, all of these simulation were run for only 5 μs due to expensive computational time and also capture all the distinctive features of free surface velocities.

Although, this work was able to achieve its objectives, there were certain areas which need to be further explored. Following recommendations will provide a tentative guideline to explore and improve this work.

1. This work was focused on to explore the plastic deformation of materials by using gas gun experiments with Lexan projectile. It would be interesting to design shock experiments with similar materials of projectile and target.
2. MPDV system was used to capture velocimetry data in all experiments. Representation of MPDV data is still one of the exploratory research.
3. Experiments were simulated using SPH technique. Alternate way to simulate these experiments need to be explored.
4. In all simulation models, Johnson-Cook material model was used with Mie-Gruneisen EOS model. Parameters of these models were used from existing literature. It is desirable to derive those experimental parameters in fundamental shock physics experiment.
5. Spall strength parameter was calculated using a uniaxial assumption. Hence, further study in spall strength in asymmetric shock experiments will definitely help to understand these materials deformation behavior and improve these simulation results.

APPENDIX A PHYSICAL MEASUREMENT OF CRATER AND BULGE

After each experiment, crater diameter, depth and bulge on the back side of target plates were measured using a slide calipers and ruler. The distance between the peak point of the bulge and flat surface of the plate was considered as the height of the bulge. Measurements were taken three times to get an average value. Figure A.1 shows the procedure of documenting all the crater and bulge dimensions.

Crater diameter measurement

Depth of penetration measurement

Bulge measurement

Figure A.1 Physical Measurement of All Impacted Plates

APPENDIX B CALCULATION OF PROBE DISTANCE FROM IMPACT CENTER

After each MPDV experiment, target plates were monitored for impact center location and probe distances were measured corresponding to impact center. Both impact center and probe # 1 location were measured initially respective to plate center. Plate center was considered as datum (i.e. (0,0)) coordinates. Impact center location was initially measured in Cartesian coordinate system and then converted to Polar coordinate system to get a better idea of impact center location corresponding to plate center. Similarly, probe # 1 location was measured in Cartesian system and then converted to Polar coordinates for measurement.

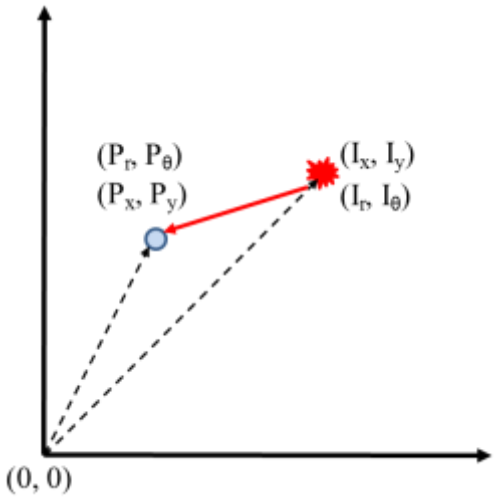

Figure B.B.1 Schematic of Probe Location and Impact Center

Here, ‘Red’ dot represents impact center whereas ‘Blue’ dot represents Probe # 1 location. Plate center is located in the origin (0,0).

In the above figure, (I_x, I_y) represents impact center location in Cartesian coordinate system whereas (I_r, I_θ) represents impact center location in Polar coordinate system. Similarly, (P_x, P_y) and (P_r, P_θ) represent the probe # 1 location respectively.

Distance between impact center and probe # 1 were calculated using following equation:

$$D = \sqrt{\{(I_x - P_x)^2 + (I_y - P_y)^2} \quad \text{(B1)}$$

Similarly, rest of the probe locations were calculated based on Probe # 1 location and plate center. Then, probe distances from impact center were calculated. Typical impact center relative to the probe arrays are shown in following figures.

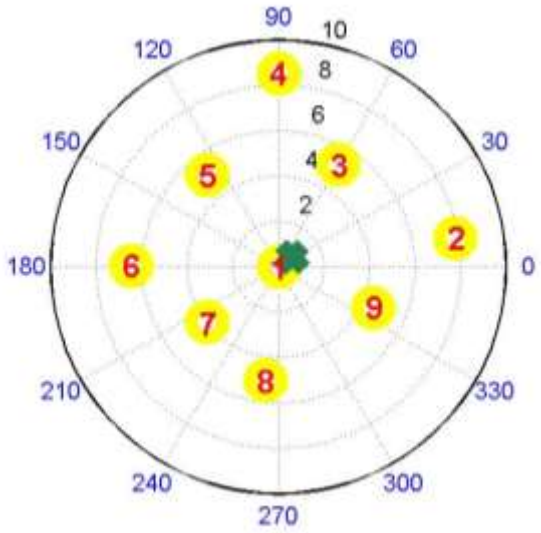

Figure B.B.2 Impact Center and Probe Array in a Typical 9-Probe MPDV Experiment (Impact Velocity: 4.763 km/s)

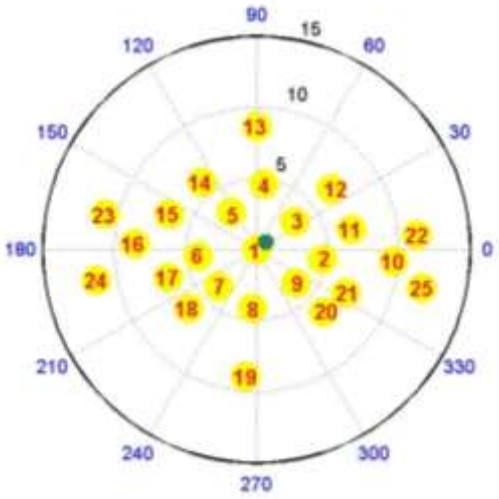

Figure B.3 Impact Center and Probe Array in a Typical 25-Probe MPDV Experiment (Impact Velocity: 4.823 km/s)

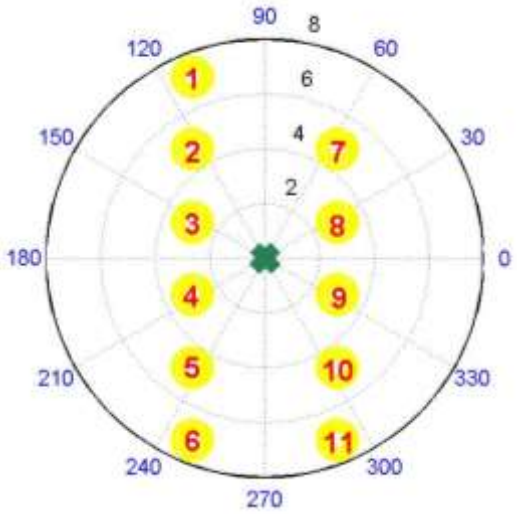

Figure B.4 Impact Center and Probe Array in a Typical 11-Probe MPDV Experiment for HY100 Steel (Impact Velocity: 6.689 km/s)

APPENDIX C SAMPLE MATLAB CODE TO CALCULATE PROBE DISTANCE FROM IMPACT CENTER

```
% All units are in mm

%--------------------------------------------------------------------
% 9-channel Probe Meterology
%--------------------------------------------------------------------

% Date: 05-20-2013
% Impact Velocity: 4.763 km/s

%--------------------------------------------------------------------

% Plate center (C)

Cx = 0;
Cy = 0;

%--------------------------------------------------------------------
% Impact Center (IC)
%--------------------------------------------------------------------

IC_x = 76.2-71.73;%74.1;
IC_y = 76.2-73.05;%74.8;

%--------------------------------------------------------------------
% Probe Center (PP)
%--------------------------------------------------------------------

P1_x = 76.2-71.77;%76.5;
P1_y = 76.2-72.31;%72.4;


%--------------------------------------------------------------------
% degree to radian conversion
%--------------------------------------------------------------------

d2r = pi/180;
```

```
%-------------------------------------------------------------------------------
% Location of all probes respective to probe center P1(polar coordinate)
%-------------------------------------------------------------------------------

Pr = 10.*[0,0.785,0.521,0.850,0.511,0.648,0.396,0.502,0.452];
Pth = d2r*[0,9.4,59.6,89.9,127.5,179.5,218.0,263.8,336.4];


%-------------------------------------------------------------------------
% Converting all probe locations into Cartesian coordinates
% respective to probe center (P1)
%-------------------------------------------------------------------------

for i=Pr(1):Pr(9), %j= Pth(1):Pth(25)
[PX,PY] = pol2cart(Pth,Pr);
end

%-------------------------------------------------------------------------
% Coordinates of all probes from plate center
%-------------------------------------------------------------------------

Px = PX+P1_x;
Py = PY+P1_y;

%-------------------------------------------------------------------------
% Distance of all probes from impact center
%-------------------------------------------------------------------------

L = sqrt(((IC_x-Px).*(IC_x-Px))+((IC_y-Py).*(IC_y-Py)));
Lc = (L.');

%-------------------------------------------------------------------------
% Plot all co-ordinates
%-------------------------------------------------------------------------

polar(Pth,Pr,'ro');
labels = cellstr(num2str([1:9]'));
text(Pth,Pr(i),labels(i))
```

APPENDIX D SAMPLE MATLAB PROGRAM TO GROUP ALL THE MPDV PROBE VELOCITIES

```
close all
clear all
load('RunData_Run06.mat');


% ------------------------------------------------------------------------
% correcting time data for plot
% ------------------------------------------------------------------------

E1  = (RunData{1,3}(:,1))-(5.1211e-05);%C85
E2  = (RunData{2,3}(:,1))-(5.1211e-05);%C248
E3  = (RunData{3,3}(:,1))-(5.1211e-05);%C223
E4  = (RunData{4,3}(:,1))-(5.1211e-05);%C247
E5  = (RunData{5,3}(:,1))-(5.1211e-05);%C287
E6  = (RunData{6,3}(:,1))-(5.1211e-05);%C280
E7  = (RunData{7,3}(:,1))-(5.1211e-05);%C252
E8  = (RunData{8,3}(:,1))-(5.1211e-05);%C232
E9  = (RunData{9,3}(:,1))-(5.1211e-05);%C201

% ------------------------------------------------------------------------
% defining velocity data for plot
% ------------------------------------------------------------------------

V1  = (RunData{1, 3}(:,2));
V2  = (RunData{2, 3}(:,2));
V3  = (RunData{3, 3}(:,2));
V4  = (RunData{4, 3}(:,2));
V5  = (RunData{5, 3}(:,2));
V6  = (RunData{6, 3}(:,2));
V7  = (RunData{7, 3}(:,2));
V8  = (RunData{8, 3}(:,2));
V9  = (RunData{9, 3}(:,2));




% ------------------------------------------------------------------------

% Adjust time and Velocity.
% Start all curves at the next point after negative values

% ------------------------------------------------------------------------
```

```
% Time Adjustment|
%--------------------------------------------------------------------------


TG1=E1;

TG7=E7(251:251+1800);
TG9=E9(201:201+1800);

TG3=E3(223:223+1800);
TG5=E5(286:286+1800);
TG8=E8(232:232+1800);

TG2=E2(244:244+1800);
TG4=E4(245:245+1800);
TG6=E6(274:274+1800);


%--------------------------------------------------------------------------
% Velocity Adjustment
%--------------------------------------------------------------------------

VG1=V1;

VG7=V7(251:251+1800);
VG9=V9(201:201+1800);
VG79=(VG7+VG9)/2;

VG3=V3(223:223+1800);
VG5=V5(286:286+1800);
VG8=V8(232:232+1800);
VG358 = (VG3+VG5+VG8)/3;

VG2=V2(244:244+1800);
VG4=V4(245:245+1800);
VG6=V6(274:274+1800);
VG246 = (VG2+VG4+VG6)/3;
```

APPENDIX E SAMPLE COMMAND SCRIPT TO CREATE SPH MODEL

This sample script command allows to create a simple axisymmetric plate and projectile model in LS-DYNA SPH solver. All units are in m, Kg/m^3. Here x,y,z represents the corresponding coordinates of rectangular box (i.e. plate and projectile), Nx, Ny, Nz represent the number of SPH elements on x-,y-,z-axis and Rx, Ry, Rz represents rotational coordinates.

```
$# LS-PrePost command file created by LS-PrePost 3.2 - 27Jan2013(17:00) -64bit-Window
$# Created on May-12-2014 (14:04:28)
genselect target part
genselect clear
$# plate A36
$#              x1          y1          z1          x2          y2          z2        Nx/Ny/Nz   Scale
sphgen box 0.000000 0.000000 -1.000000 0.076200 0.012700 1.000000 1524/254/1 100.000000
$# Rx          Ry          Rz
0.000000 0.000000 0.000000
$#                Part ID    Node ID    Density
sphgen accept   1          1000001     7890       0 0
$# projectile Lexan
```

genselect clear

sphgen box 0.00 0.013700 -1.000000 0.002780 0.022310 1.000000 24/60/1 100.000000

0.000000 0.000000 0.000000

sphgen accept 2 10001 1190 0 0

APPENDIX F SPH PARTICLE SPACING STUDY

SPH simulation is vastly dependent on the SPH particle spacing. Typical dense particle model will give much finer results. But, SPH algorithm is highly expensive in terms of computational resources and time; hence there is a trade-off for dense particle spacing.

In this work, all gas gun experiments were simulated using SPH method. Extensive particle spacing study was conducted before creating the final model of projectile and target plate. Figure E1 shows a typical results of particle spacing study for a typical 9-probe experiment. Free surface velocity of the probe group closest to the impact center was considered only.

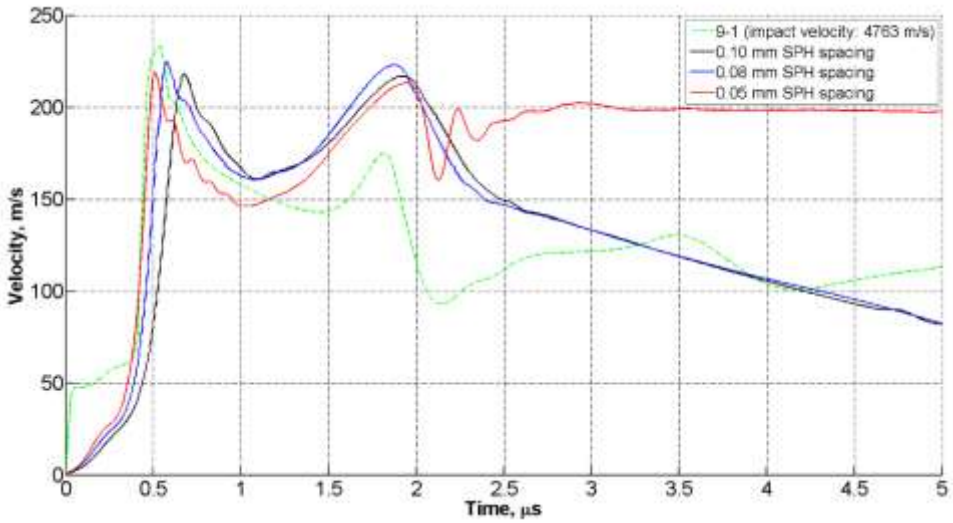

Figure F.1 Typical SPH Particle Spacing Study of a 9-probe MPDV Experiment

This figure clearly showed that with a denser particle spacing; LS-DYNA models were able to capture all the basic features of A36 steel. Hence, all the further models of A36 steel were

developed with a particle spacing of 0.05 mm for target material. Particle spacing for Lexan projectiles were selected such that mass of each SPH particle in Lexan projectile were equal to the mass of particles in the target plate.

REFERENCES

[1] Doolan C. A Two-Stage Light Gas Gun for the Study of High Speed Impact in Propellants. Salisbury: 2001.

[2] Chhabildas LC, Knudson MD. Techniques to Launch Projectile Plates to Very High Velocities. In: Chhabildas LC, Davidson L, Horie Y, editors. High-Pressure Shock Compression Solids VIII, Springer-Verlag Berlin Heidelberg; 2005, p. 143–99. doi:10.1007/3-540-27168-6_4.

[3] Holmes N. "Shocking" Gas-Gun Experiments. S TR 2000:13–9.

[4] Swift HF. Light-Gas Gun Technology : A Historical Perspective. In: Chhabildas LC, Davison L, Horie Y, editors. High-Pressure Shock Compression Solids VIII, Springer-Verlag Berlin Heidelberg; 2005, p. 1–35.

[5] Rosenberg Z, Dekel E. Terminal Ballistics. Springer; 2012.

[6] Oscarson JH, Graff KF. Spall fracture and dynamic response of materials. Columbus, OH: 1968.

[7] Corbett GG, Reid SR, Johnson W. Impact loading of plates and shells by free-flying projectiles: A review. Int J Impact Eng 1996;18:141–230.

[8] Goldsmith W, Liu TW, Chulay S. Plate impact and perforation by projectiles. Exp Mech 1965;5:385–404. doi:10.1007/BF02327429.

[9] Christman DR, Gehrig JW. Analysis of High-Velocity Projectile Penetration Mechanics. J Appl Phys 1966;37:1579. doi:10.1063/1.1708570.

[10] Shockey DA, Curran DR, De Carli PS. Damage in steel plates from hypervelocity impact. I. Physical changes and effects of projectile material. J Appl Phys 1975;46:3766–75. doi:10.1063/1.322162.

[11] Bond JW. Hypervelocity Impact Shock Induced Damage to Steel Armor. Fort Belvoir, Virginia: 1976.

[12] Merzhievskii LA, Titov VM. Perforation of plates through high velocity impact. J Appl Mech Tech Phys 1975;16:757–64.

[13] Johnson GR, Cook WH. A constitutive model and data for metals subjected to large strains, high strain rates and high temperatures. 7th Int. Symp. Ballist., The Hague, Netharlands: 1983, p. 541–7.

[14] Sorensen BR, Kimsey KD, Silsby GF, Schffler DR, Sherrick TM, Rosset WS. High Velocity Penetration of Steel Targets. Int J Impact Eng 1991;11:107–19.

[15] Anderson CE, Hohler V, Walker JD, Stilp AJ. Time-Resolved Penetration of Long Rods into Steel Targets. Int J Impact Eng 1995;16:1–18.

[16] Børvik T, Clausen AH, Hopperstad OS, Langseth M. Perforation of AA5083-H116 aluminium plates with conical-nose steel projectiles—experimental study. Int J Impact Eng 2004;30:367–84. doi:10.1016/S0734-743X(03)00072-1.

[17] Barker LM, Hollenbach RE. Laser interferometer for measuring high velocities of any reflecting surface. J Appl Phys 1972;43:4669–75. doi:10.1063/1.1660986.

[18] Barker LM, Hollenbach RE. Shock wave study of the α ⇄ ε phase transition in iron. J Appl Phys 1974;45:4872. doi:10.1063/1.1663148.

[19] Kuscher GF, Hohler V, Stilp AJ. High-resolution velocity interferometer system for any reflector (VISAR) laser interferometer measurements of the rear side response of impact loaded steel plates. High Speed Photogr 1983;348:508–13.

[20] Wise JL, Chhabildas LC. Laser Interferometer Measurements of Refractive Index in Shock-Compressed Materials. In: Gupta YM, editor. Proc. Fourth Am. Phys. Soc. Trop. Conf. Shock Waves Condens. Matter, Spokane, WA: Plenum Press; 1986, p. 441–54.

[21] Forrestal MJ, Lee LM, Jenrette BD. Laboratory-Scale Penetration Experiments Into Geological Targets to Impact Velocities of 2.1 km/s. J Appl Mech 1986;53:317. doi:10.1115/1.3171758.

[22] Rosenberg Z, Bless SJ. Determination of dynamic yield strengths with embedded manganin gages in plate-impact and long-rod experiments. Exp Mech 1986;26:279–82. doi:10.1007/BF02320054.

[23] Zurek AK, Thissell WR, Johnson JN, Tonks DL, Hixson R. Micromechanics of Spall and Damage in Tantalum. J Mater Process Technol 1996;60:261–7.

[24] Knudson MD, Hanson DL, Bailey JE, Hall CA, Asay JR. Equation of State Measurements in Liquid Deuterium to 70 GPa. Phys Rev Lett 2001;87:225501. doi:10.1103/PhysRevLett.87.225501.

[25] Vogler T, Clayton J. Heterogeneous deformation and spall of an extruded tungsten alloy: plate impact experiments and crystal plasticity modeling. J Mech Phys Solids 2008;56:297–335. doi:10.1016/j.jmps.2007.06.013.

[26] Mukherjee D, Rav A, Sur A, Joshi KD, Gupta SC. Shock induced spall fracture in polycrystalline copper. AIP Conf. Proc. 1591, vol. 608, AIP Publishing; 2014, p. 608–10. doi:10.1063/1.4872691.

[27] Dolan DH. Foundations of VISAR analysis. Albuquerque, New Mexico, USA: 2006.

[28] Strand OT, Goosman DR, Martinez C, Whitworth TL, Kuhlow WW. Compact system for high-speed velocimetry using heterodyne techniques. Rev Sci Instrum 2006;77:083108:1–9. doi:10.1063/1.2336749.

[29] Jilek B. History of Velocimetry Technology. In: Albuquerque N, editor. 7th Annu. PDV Work., Sandia National Laboratories; 2012.

[30] Chau R, Stolken J, Kumar M, Holmes NC. Shock Hugoniot of Single Crystal Copper. J Appl Phys 2010;107:023506.

[31] Daykin E, Perez C. Techniques and Tools for PDV Applications: A Work in Progress, 2008.

[32] Daykin E. Photonic Doppler Velocimetry Multiplexing Techniques : Evaluation of Photonic Technologies n.d.:1.

[33] Danielson JR, Daykin EP, Diaz a B, Doty DL, Frogget BC, Furlanetto MR, et al. Measurement of an explosively driven hemispherical shell using 96 points of optical velocimetry. J Phys Conf Ser 2014;500:142008. doi:10.1088/1742-6596/500/14/142008.

[34] Turley WD, Daykin E, Hixson R, LaLone BM, Perez C, Stevens GD, et al. Copper spall experiments with recompression using HE (Copper Spall Soft Recovery Experiments). 8th Annu. PDV Work., Las Vegas, NV: 2014.

[35] Ao T, Dolan DH. Effect of window reflections on photonic Doppler velocimetry measurements. Rev Sci Instrum 2011;82:023907. doi:10.1063/1.3551954.

[36] Børvik T, Langseth M, Hopperstad OS, Malo K a. Ballistic penetration of steel plates. Int J Impact Eng 1999;22:855–86. doi:10.1016/S0734-743X(99)00011-1.

[37] Børvik T, Hopperstad OS, Berstad T, Langseth M. Numerical simulation of plugging failure in ballistic penetration. Int J Solid Struct 2001;38:6241–64.

[38] Chen XW, Li QM. Perforation of a thick plate by rigid projectiles. Int J Impact Eng 2003;28:743–59. doi:10.1016/S0734-743X(02)00152-5.

[39] Chen XW, Yang YB, Lu ZH, Chen YZ. Perforation of metallic plates struck by a blunt projectile with a soft nose. Int J Impact Eng 2008;35:549–58. doi:10.1016/j.ijimpeng.2007.05.002.

[40] Chen XW, Zhou XQ, Li XL. On perforation of ductile metallic plates by blunt rigid projectile. Eur J Mech - A/Solids 2009;28:273–83. doi:10.1016/j.euromechsol.2008.07.002.

[41] Eftis J, Nemes JA. Modeling of impact-induced spall fracture and post spall behavior of a circular plate. Int J Fract 1992;53:301–24.

[42] Zukas JA. High velocity impact dynamics. vol. 1990. Wiley; 1990.

[43] Rolsten RF, Huntf HH. Phenomena Resulting from Hypervelocity Impact. J Spacecracft 1964;2:38–43.

[44] Hayhurst CJ, Ranson HJ, Gardner DJ, Birnbaum NK. Modeling of microparticle hypervelocity oblique impacts on thick plates. Int J Impact Eng 1995;17:375–86.

[45] Grady DE, Kipp ME. Experimental and computational simulation of the high velocity impact of copper spheres on steel plates. Int J Impact Eng 1994;15:645–60. doi:10.1016/0734-743X(94)90144-A.

[46] Martineau RL, Prime MB, Duffey T. Penetration of HSLA-100 Steel with Tungsten Carbide Spheres at Striking Velocities Between 0 . 8 and 2 . 5 km / sec. Int J Impact Eng 2004;30:505–20.

[47] Shukla A, Ravichandran G, Rajapakse YDS. Dynamic Failure of Materials and Structures. New York, USA: Springer; 2010.

[48] Shah QH, Abakr YA. Effect of distance from the support on the penetration mechanism of clamped circular polycarbonate armor plates. Int J Impact Eng 2008;35:1244–50. doi:10.1016/j.ijimpeng.2007.07.012.

[49] Swaddiwudhipong S, Islam MJ, Liu ZS. High Velocity Penetration/Perforation Using Coupled Smooth Particle Hydrodynamics-Finite Element Method. Int J Prot Struct 2010;1:489–506.

[50] O'Daniel J, Danielson K, Boone N. Modeling fragment simulating projectile penetration into steel plates using finite elements and meshfree particles. Shock Vib 2011;18:425–36. doi:10.3233/SAV-2010-0523.

[51] Kalameh HA, Karamali A, Anitescu C, Rabczuk T. High velocity impact of metal sphere on thin metallic plate using smooth particle hydrodynamics (SPH) method. Front Struct Civ Eng 2012;6:101–10. doi:10.1007/s11709-012-0160-z.

[52] Zukas J. Introduction to Hydrocodes. Elsevier; 2004.

[53] Lucy LB. A numerical approach to the testing of the fission hypothesis. Astron J 1977;82:1013. doi:10.1086/112164.

[54] Gingold RA, Monaghan JJ. Smoothed particle hydrodynamics-theory and application to non-spherical stars. Mon Not R Astron Soc 1977;181:375–89.

[55] Monaghan JJ. Particle methods for hydrodynamics. Comput Phys Reports 1985;3:71–124. doi:10.1016/0167-7977(85)90010-3.

[56] Monaghan JJ. Smoothed Particle Hydrodynamics. Annu Rev Astron Astrophys 1992;30:543–74.

[57] Monaghan JJ. Smoothed particle hydrodynamics. Reports Prog Phys 2005;68:1703–59. doi:10.1088/0034-4885/68/8/R01.

[58] Monaghan JJ. On the problem of penetration in particle methods. J Comput Phys 1989;82:1–15. doi:10.1016/0021-9991(89)90032-6.

[59] Libersky LD, Petschek AG. Smooth Particle Hydrodynamics with Strength of Materials. In: Trease HE, Fritts MF, Crowley WP, editors. Adv. Free. Method Incl. Contrib. Adapt. Gridding Smooth Part. Hydrodyn. Method, vol. 395, Berlin, Heidelberg: Springer Berlin Heidelberg; 1991, p. 248–57. doi:10.1007/3-540-54960-9.

[60] Plassard F, Mespoulet J, Hereil P. Hypervelocity impact of aluminium sphere against aluminium plate : experiment and LS-DYNA correlation. 8th Eur. LS-DYNA Users Conf., Strasbourg, Germany: 2011, p. 1–11.

[61] Schwer L. Optional Strain-Rate Forms for the Johnson Cook Constitutive Model and the Role of the Parameter Epsilon _ 01. 6th Eur. LS_DYNA Users' Conf., Gothenburg, Sweden: ERAB; 2007, p. 1–17.

[62] Jackson KE, Fuchs YT. Comparison of ALE and SPH Simulations of Vertical Drop Tests of a Composite Fuselage Section into Water. 10th Int. LS-DYNA® Users Conf., Dearbon, Michigan: 2010, p. 1–20.

[63] Somasundaram D, Trabia M, O'Toole B, Hixson R. Variables Affecting Smoothed Particle Hydrodynamics Simulation Of High Velocity Flyer Plate Impact Experiments. In: Schleyer G, Brebbia CA, editors. Struct. Under Shock Impact XIII, The New Forest, UK: WIT press; 2014, p. 8.

[64] Katayama M, Kibe S, Toda S. A Numerical Simulation Method and Its Validation For Debris Impact Against The Whipple Bumper Shield. Int J Impact Eng 1995;17:465–76.

[65] Seidt JD, Gilat A, Klein JA, Leach JR. High Strain Rate , High Temperature Constitutive and Failure Models for EOD Impact Scenarios. SEM Annu. Conf. Expo. Exp. Appl. Mech., Society for Experimental Mechanics, Inc.; 2007, p. 15.

[66] Littlewood DJ. Simulation of Dynamic Fracture Using Peridynamics, Finite Element Modeling, and Contact. ASME 2010 Int. Mech. Eng. Congr. Expo., Vancouver, British Columbia, Canada: ASME; 2010, p. 1–9. doi:10.1115/IMECE2010-40621.

[67] Elshenawy T, Li QM. Influences of target strength and confinement on the penetration depth of an oil well perforator. Int J Impact Eng 2013;54:130–7. doi:10.1016/j.ijimpeng.2012.10.010.

[68] LS-DYNA® Theory Manual. vol. 15. 2015th ed. LSTC; 2015.

[69] Xue Q, Nesterenko VF, Meyers MA. Evaluation of the collapsing thick-walled cylinder technique for shear-band spacing. Inetrnational J Impact Eng 2003;28:257–80.

[70] Holmquist TJ. Strength and Fracture Characteristics of HY-80, HY-100, and HY- 130 Steels Subjected to Various Strains, Strain Rates, Temperatures, and Pressures. Silver Spring, MD: 1987.

[71] LS-DYNA® KEYWORD USER ' S MANUAL. vol. I. 971st ed. LIVERMORE SOFTWARE TECHNOLOGY CORPORATION (LSTC); 2007.

[72] Zocher MA, Maudlin PJ, Chen SR, Flower-Maudlin EC. An Evaluation of Several Hardening Models using Taylor Cylinder Impact Data. Eur. Congr. Comput. Methods Appl. Sci. Eng., vol. 53, Barcelona, Spain: ECCOMAS; 2000, p. 1–20. doi:10.1063/1.882984.

[73] Steinberg DJ. Equation of State and Strength Properties of Selected Materials. Livermore, California: 1996.

[74] Danyluk J. An Analysis of Multi-Material Plates Under Explosive Loading. Rensselaer Polytechnic Institute, 2011.

[75] Banerjee B. Material point method simulations of fragmenting cylinders. 17th ASCE Eng. Mech. Conf., vol. 1, Newark, DE: 2012, p. 15.

[76] Hammond RI, Proud WG. Does the pressure-induced α – ε phase transition occur for all low-alloy steels ? Proc R Soc London Ser A Math Phys Eng Sci 2004;460:2959–74. doi:10.1098/rspa.2004.1314.

[77] Selwa M, Crystalline Phase Change in Steel Alloys Due to High Speed Impact, PhD Dissertation, 2015.

VITA

Graduate College
University of Nevada, Las Vegas

Shawoon Kumar Roy

Degree:

Bachelor of Science, Materials and Metallurgical Engineering (2008)
Bangladesh University of Engineering and Technology
Dhaka, Bangladesh 1000

Master of Science, Materials and Nuclear Engineering (2011)
University of Nevada, Las Vegas
Las Vegas, NV

Publications (from this work)

Journal Articles:

- O'Toole B, Trabia M, Hixson R, Roy SK, Peña M, Becker S, et al. Modeling Plastic Deformation of Steel Plates in Hypervelocity Impact Experiments. Procedia Eng 2015;103:458–65. doi:10.1016/j.proeng.2015.04.060. (presented in HVIS 2015 conference)

- Pena, M., Becker, S., Garza, A., Hanache, M., Hixson, R., Jennings, R., ... & Trabia, M. (2015). Many Point Optical Velocimetry for Gas Gun Applications. Bulletin of the qAmerican Physical Society, 60.

- Roy SK, Trabia M, OToole B, Hixson R, Becker S, Peña M, et al. Study of Hypervelocity Projectile Impact on Thick Metallic Plates. Manuscript in revision in Shock and Vibration (2015).

Book Chapter:

- S. Roy, B. O'Toole, M. Trabia, R. Hixson, M. Pena, S. Becker, E. Daykin, E. Machorro, R. Jennings, M. Matthes, "Use of a Multiplexed Photonic Doppler Velocimetry (MPDV) System to Study Plastic Deformation of Metallic Steel Plates in High Velocity Impact," Fracture, Fatigue, Failure and Damage Evolution, Volume 8, Springer Verlag 2015. (presented in SEM 2015 Annual Conference)

Technical Reports:

- Plastic Deformation Study Using a Light Gas Gun', Site-Directed Research & Development Fiscal Year Report, NSTec (2013, 2014).

Conferences & Presentations:

- M. Pena, M. Trabia, B. O'Toole, R. Hixson, S.K. Roy, S. Becker, R. Jennings, M. Matthes, M. Walling, E. Daykin, "Use of Multiplexed Photonic Doppler Velocimetry (MPDV) System to Study Plastic Deformation of Metallic Steel Plates in High Velocity Impact", SEM 2015 Annual Conference & Exposition on Experimental and Applied Mechanics, Costa Mesa, CA, June 8-11, 2015.

- M. Trabia, B. O'Toole, S. Roy, D. Somasoundarum, R. Jennings, M. Matthes, R. Hixson, S. Becker, E. Daykin, M. Pena, E, Machorro, "Computational model verification using multiplexed photonic doppler velocimetry for high-velocity projectile impact on steel targets," International Conference on Multiscale Materials Modeling 2014, Berkeley, CA, October, 2014.

- S. Roy, B. O'Toole, M. Trabia, R. Jennings, M. Matthes, M. Pena, E. Daykin, R. Hixson, S. Becker, C. Perez, E. Machorro, "Use of Multiplexed Photonic Doppler Velocimetry (MPDV) in Measuring Plastic Deformation of Plates under Hypervelocity Condition," PDV Workshop 2014, Las Vegas, NV, June 2014.

- M. Trabia, B. O'Toole, S. Roy, D. Somasoundarum, R. Jennings, M. Matthes, R. Hixson, S. Becker, E. Daykin, M. Pena, E, Machorro, "An Approach for Measuring and Modeling of Plastic Deformation of Metallic Plates During High Velocity Impact," NAFEMS Americas Conference, Colorado Springs, CO, May 2014.

- S. Roy, "Plastic Deformation of Steel Plates under High Velocity Impact", UNLV-NSTech Symposium, Las Vegas, NV, March 2014.

- S. Roy, M. Trabia, B. O'Toole, J. Thota, R. Jennings, D. Somasandaram, M. Mathes, S. Becker, E. Daykin, R. Hixson, E. Machorro, T. Meehan, M. Pena, C. Perez, N. Snipe, K. Crawford, and S. Gardner, "Plastic Deformation of Steel Plates under High Impact Loading," 84th Shock & Vibration Symposium, Atlanta, GA, November, 2013.

- M. Trabia, B. O'Toole, J. Thota, R. Jennings, D. Somasundaram, S. Roy, S. Becker, E. Daykin, R. Hixson, "Computational Simulation and Experimental Study of Plastic Deformation in A36 Steel during High Velocity Impact," ASME Verification & Validation Symposium, Las Vegas, Nevada, May 2013.

Dissertation Title:

An Approach to Model Plastic Deformation of Metallic Plates in Hypervelocity Impact Experiments

Dissertation Committee:

Co-Chairperson, Dr. Mohamed Trabia, Ph.D.

Co-Chairperson, Dr. Brendan O'Toole, Ph.D.

Committee Member, Dr. Yitung Chen, Ph.D.

Committee Member, Dr. Zhiyong Wang, Ph.D.

Committee Member, Dr. William Culberth, Ph.D.

Committee Member, Dr. Robert Hixson, Ph.D.

Graduate College Representative, Dr. Rama Venkat, Ph.D.